Spectrochimica Acta Part B: Atomic Spectroscopy 201 (2023) 106627

Contents lists available at ScienceDirect

Spectrochimica Acta Part B: Atomic Spectroscopy

journal homepage: www.elsevier.com/locate/sab

Radiation influence on the plasma atomic kinetics and spectra in experiments on radiative shock waves

R. Rodríguez *, G. Espinosa-Vivas, J.M. Gil

IUNAT, Departamento de Física, Universidad de Las Palmas de Gran Canaria, 35017 Las Palmas de Gran Canaria, Spain

ARTICLE INFO

Keywords:
Plasma radiative properties and atomic spectra of photoionized plasmas
Radiative precursors of radiative shocks experiments
Atomic kinetics, radiation transport and atomic spectra simulations

ABSTRACT

Radiative shocks waves are among of the most interesting astrophysical phenomena and due to their relevance, many laboratory experiments, using high-power lasers, have been performed to achieve a better understanding of them. The radiation emitted by the shock front can heat and ionize the pre-shock medium leading to the formation of radiative precursors, which are relevant in these phenomena since they absorb part of the radiation emitted by the shock front and becomes a strong source of radiation emission. The plasma in the precursor can be considered as a photoionized plasma in which the external radiation field plays a dominant role in the atomic kinetics behavior. A numerical study of the influence of the radiation field on the ion populations, radiative properties and atomic spectra of radiative precursors in radiative shocks generated in two laboratory experiments is presented. For the numerical simulations, three types of collisional-radiative models have been used. In the first one, the radiation induced processes are not included. In the second type, the radiative atomic processes induced by plasma self-absorption are considered. Finally, the radiative processes induced by both the external radiation field and the plasma self-absorption are included. The results obtained show the noticeable influence of the radiation field on the plasma properties analyzed.

1. Introduction

In the last three decades there has been considerable progress in the field of high energy density (HED) laboratory astrophysics. This has been made possible, on the one hand, by the considerable development of high-energy-density facilities [1], such as high-power lasers and fast magnetic pinch generators, and, on the other hand, by the possibility of scaling the magnetohydrodynamics between laboratory and astrophysical scenarios [2–6]. The experiments carried out in the laboratory allow both to reproduce conditions identical to certain astrophysical phenomena or scenarios or to recreate hydrodynamically scaled versions of others. The experiments present the advantage of being repeatable and that the initial conditions are controllable, and permit to explain and predict what occurs in astrophysical situations. Besides, they also provide useful data for verification and validation of numerical codes used in the simulation of HED plasmas.

Radiative shock waves are among the most interesting astrophysical phenomena and they are ubiquitous throughout the universe, being observed, for example, in accretion shocks [7], supernova remnants [8], pulsating stars [9] and at the head of stellar jets [10], and they also play a fundamental role in energy transport in the interstellar medium [11]. They are strong shocks that reach high temperatures and are the source of intense radiation [12]. Depending on the opacity of the medium in which they propagate, the radiation emitted by the shock front can heat and ionize the pre-shock medium leading to the formation of a radiative precursor [13]. Due to their relevance in Astrophysics, many laboratory experiments, using high-power lasers, have been performed to achieve a better understanding of them [12,14–24], using noble gases as a target. Depending of the type of experiment, the laser intensities on the target are comprised between 10^{14} and 10^{17} Wcm^{-2}, with shock speeds ranging between 10 and 150 kms^{-1} and matter densities and plasma temperatures from 10^{-5} to 10^{-1} gcm^{-3} and from 1 to 50 eV, respectively.

The radiative precursors play a relevant role when they are generated, since they absorb part of the radiation emitted by the shock front and, in turn, become a strong source of radiation emission. Therefore, a proper description of the radiative shock wave phenomenon have to take into account the effects of the radiative absorption by the matter and the radiation emitted by the shock front in a coupled form. This has recently made it possible to explain a discrepancy between the accretion

* Corresponding author.
E-mail address: rafael.rodriguezperez@ulpgc.es (R. Rodríguez).

https://doi.org/10.1016/j.sab.2023.106627
Received 21 October 2022; Received in revised form 12 January 2023; Accepted 16 January 2023
Available online 20 January 2023

rates obtained from UV and X-ray observations during the impact of a column of matter on the surface of a Classical T Tauri star [25], for example.

Since the radiative precursor is generated by the radiation emitted from the shock front, the plasma in the precursor can be considered as a photoionized plasma. Photoionized plasmas are those in which the radiation is sufficiently intense that photoexcitation and ionization rates are high relative to electron collisional and excitation rates [26]. Therefore, radiation plays a dominant role in the atomic kinetics behavior, participating or even dominating the ionization balance and the distribution of the ion populations [27]. Photoionized plasmas are usually referred as overionized since their average ionization is larger than at of collisional dominated plasma [28]. They are very common in Astrophysics, in pulse-power devices and laser-produced plasmas.

In the laboratory experiments, the diagnostics of the plasma parameters, such as the density, the electron temperature and ionization state, is essential to characterize the radiative precursors. Since the plasma emission spectrum contains information about the local instantaneous density and temperature, atomic emission spectroscopy diagnostic is a very useful tool to determine the plasma conditions and is frequently used [29–38] since it is comparatively non-invasive and easy to implement. The emission spectroscopy diagnostics of the plasma parameters is based on comparison of the synthetic spectra with those obtained experimentally. The generation of the synthetic spectra for given plasma conditions rely on the calculation of the atomic level populations and the plasma radiative properties, i.e. the absorption coefficient and the emissivity. Furthermore, these properties are also essential in radiation-hydrodynamic simulations of these plasmas. Therefore, atomic kinetics and radiative properties calculations are crucial in modeling HED plasmas.

Due to the relevance of the radiative processes, the plasmas in the radiative precursor are in non-local thermodynamic equilibrium (NLTE). In this thermodynamic regime, the atomic level populations in the plasma are obtained by solving a set of coupled rate equations in the called collisional-radiative (CR) models [39], which include the transition rates among the atomic levels due to the collisions with electrons and photons. The rates of the photon driven atomic processes are calculated through integrals over the specific intensity of the radiation field. On the other hand, the specific intensity in the plasma is commonly obtained from solving the radiative transfer equation (RTE), where the opacity and the emissivity are key quantities which, in turn, depend on the atomic level populations. Therefore, accurate modeling of the plasmas in the radiative precursor entails a CR model coupled to the RTE, with photon escape and non-local zone-to-zone coupling in both transition lines and the continuum [40], highly non-linear, that must be solved self-consistently. The problem entails a high complexity and, due to interest in the area of HED plasmas, new developments in this field are welcomed.

In a previous work [41], the computational package MIXKIP/RAPCAL, consisting of two codes MIXKIP (MIXture KInetic Properties) devoted to the calculation of the atomic level populations in the plasmas and RAPCAL (RAdiative Properties CALculator) developed for the calculation of the radiative properties and radiation transport, was presented. This package was designed to perform fully self-consistent large-scale NLTE atomic kinetics and radiation transfer of optically thick plasmas in 1D and for 2D in cartesian geometry using the S_N method [42] in the long-characteristics scheme [43,44]. The computational package and its early versions [45,46] have been successfully applied to the calculation of plasma opacities and emissivities of optically thin 0D plasmas [47–51], charge state distribution and mean opacities of 1D thick plasmas [41,52] and K-shell plasma diagnostics [46,53,54]. In this work, the extension of MIXKIP/RAPCAL to perform simulations of the atomic kinetics and radiation transport of plasmas under the influence of external radiation fields to model photoionized plasmas is presented and its accuracy is evaluated. The model is then applied to the numerical study of the influence of the radiation emitted by the shock front on the ion ionization balance, absorption coefficient, emissivity and specific intensity of plasmas in radiative precursors generated in two radiative shock wave experiments in particular [12,17]. On the other hand, for NLTE optically thick plasmas the self-absorption can influence the ionization balance and atomic level populations and thus the radiative properties, which does not occur in LTE plasmas since their atomic kinetics is collisionally dominated and the self-absorption only affects the spectral lines in the line transport. Therefore, in this work, we also analyze the effect of the plasma self-absorption on the ion abundances, on the spectral emission and absorption coefficients and on the emission spectra.

The paper is structured as follows: in next section, we present a description of MIXKIP/RAPCAL and its extension to model photoionized plasmas. Section 3 is devoted to evaluate the accuracy of the numerical simulations of photoionized plasmas through comparisons with experimental results and numerical simulations available in the literature. In Section 4 we perform the analysis of the influence of the external radiation and the self-absorption on the ion abundances, radiative properties and specific intensities of plasmas in radiative precursors for two particular laboratory astrophysics experiments. Finally, general remarks and conclusions are collected in the last section.

2. Theoretical model

In plasmas in the NLTE regime, atomic level populations are obtained solving the rate equations of the CR models, which are given by

$$\frac{dN_{\zeta i}(\mathbf{r},t)}{dt} = \sum_{\zeta' j} N_{\zeta' j}(\mathbf{r},t) R^{+}_{\zeta' j \to \zeta i} - \sum_{\zeta' j} N_{\zeta i}(\mathbf{r},t) R^{-}_{\zeta i \to \zeta' j}, \tag{1}$$

where $N_{\zeta i}$ is the population density of the atomic level i of the ion with charge state ζ. The terms $R^{\pm}_{\zeta' j \to \zeta i}$ and $R^{\mp}_{\zeta' j \to \zeta i}$ take into account all the atomic processes, both collisional and radiative, which contribute to populate and depopulate the atomic configuration ζi, respectively. The rate coefficients of the processes that involve the collision with a free electron are obtained from the collisional cross section, $\sigma(\varepsilon_f)$ with ε_f the energy of the incident free electron, through

$$\langle v_f \sigma \rangle = \int_{E_{th}}^{\infty} v_f \sigma(\varepsilon_f) f(\mathbf{r},t,\varepsilon_f) d\varepsilon_f, \tag{2}$$

where v_f is the velocity of the incident electron, E_{th} the threshold energy of the excitation and $f(\mathbf{r},t,\varepsilon_f)$ is the energy distribution function of free electrons in the plasma. In principle, this distribution should be obtained by solving the Boltzmann equation for the free electrons which is coupled to the rate equations [55]. However, in this work, for the calculation of the collisional rates we have assumed that the free electron were thermalized and a Maxwell-Boltzmann distribution for the free electrons was used. This approximation is accurate for the plasma conditions considered in this work, since the characteristic time for the electrons to thermalize is around 1 ps which is considerably smaller than the characteristic hydrodynamic times of the experiments analyzed, which are around 1 ns [12,17].

For the radiative processes, which are essential in photoionized plasmas, the rate coefficients associated to those induced by the radiation are given by

$$\langle c\sigma \rangle = \int_{E_{th}/h}^{\infty} c\sigma(\nu) f_{ph}(\mathbf{r},t,\nu) d\nu, \tag{3}$$

with c the speed of ligth, h the Planck's constant, ν the photon frequency, $\sigma(\nu)$ the cross section of the radiative process and $f_{ph}(\mathbf{r},t,\nu)$ the energy distribution function of photons in the plasma, which is obtained from the specific intensity, $I_\nu(\mathbf{r},t,\nu,\mathbf{n})$, where $\mathbf{n}$ is a unit vector in the direction of propagation for any value of the solid angle Ω, through

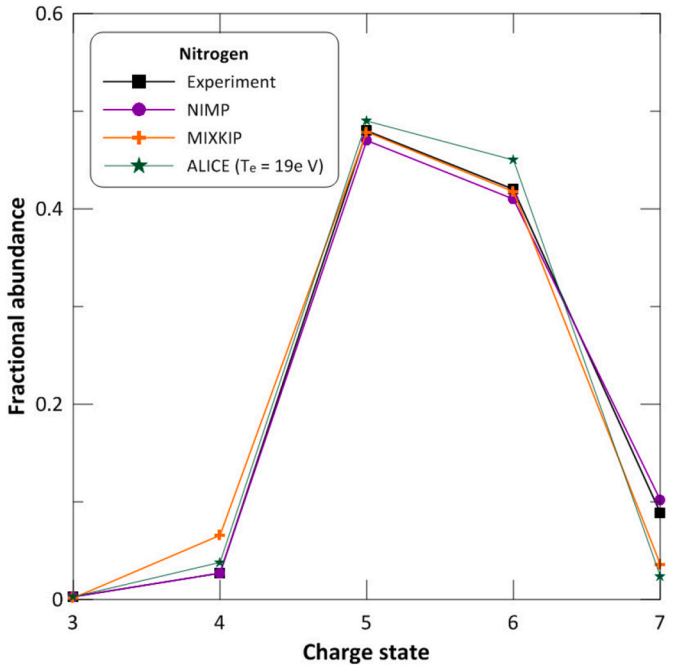

Fig. 1. Comparison of the average ionization for a nitrogen plasma at $n_i = 1.4 \times 10^{19}$ cm^{-3}, $T_e = 20$ eV and $T_{rad} = 80$ eV.

Table 1
Comparison of the average ionizations and the CSDs calculated with MIXKIP including or not the external radiation field.

	Without radiation	With radiation
$\overline{Z}$	4.77	5.41
N^{3+}	1.42×10^{-2}	5.13×10^{-3}
N^{4+}	2.01×10^{-1}	8.19×10^{-2}
N^{5+}	7.84×10^{-1}	4.45×10^{-1}
N^{6+}	3.58×10^{-11}	4.30×10^{-1}
N^{7+}	1.03×10^{-12}	3.80×10^{-2}

Table 2
Comparison of the average ionization and the radiative power loss (RPL, in ergcm^{-3} s^{-1}) of a neon plasma with simulations from the 8th NLTE Code Comparison Workshop. A Planckian radiation with temperature of 103 eV and dilution factor of 0.017 was assumed.

	$T_e = 5$ eV				$T_e = 40$ eV			
	$n_e = 10^{18}$cm^{-3}		$n_e = 10^{19}$cm^{-3}		$n_e = 10^{18}$cm^{-3}		$n_e = 10^{19}$cm^{-3}	
	$\overline{Z}$	RPL	$\overline{Z}$	RPL	$\overline{Z}$	RPL	$\overline{Z}$	RPL
MIXKIP	7.36	2.47×16	3.05	3.62×17	8.23	1.01×16	7.95	2.26×17
CODE1	7.41	8.09×16	3.06	7.94×17	8.18	1.03×16	7.94	2.19×17
CODE2	8.07	–	5.45	–	8.31	–	7.98	–
CODE3	7.53	5.81×16	3.03	5.58×17	8.25	1.03×16	7.97	2.05×17
CODE4	6.38	3.94×16	3.19	5.79×17	8.16	1.14×16	7.95	1.94×17
CODE5	3.95	–	2.42	–	8.02	–	7.94	–
CODE6	7.73	1.24×15	3.13	7.42×17	8.18	6.47×15	7.94	1.03×17

$$f_{ph}(\mathbf{r},t,\nu) = \frac{1}{4\pi}\int \frac{I_\nu(\mathbf{r},t,\nu,\mathbf{n})}{h c \nu} d\Omega. \tag{4}$$

The specific intensity is obtained by solving the RTE, which is given by

$$\frac{1}{c}\frac{\partial I_\nu(\mathbf{r},t,\nu,\mathbf{n})}{\partial t} + \mathbf{n}\cdot\nabla I_\nu(\mathbf{r},t,\nu,\mathbf{n}) = j(\mathbf{r},t,\nu) - \kappa(\mathbf{r},t,\nu) I_\nu(\mathbf{r},t,\nu,\mathbf{n}), \tag{5}$$

where $j(\mathbf{r},t,\nu)$ and $\kappa(\mathbf{r},t,\nu)$ are the plasma monochromatic emissivity and absorption coefficients, i.e. the plasma radiative properties, which are commonly assumed as isotropic. They depend, in turn, on the atomic level populations. Therefore, for optically thick plasmas, the rate equations are coupled to the RTE and they must be solved simultaneously and self-consistently. Furthermore, different regions of the plasma could be coupled through radiation and, therefore, the self-consistence should be achieved for the whole plasma.

In the present work, we are interested in the analysis of the influence of the radiation emitted by the shock front and the plasma self-absorption on the atomic kinetics and specific intensity at different positions of radiative precursors generated in laboratory experiments. As said before, in the experiments considered in this work the hydrodynamic characteristic times are around 1 ns, and the electron densities and temperatures are ranged between $10^{18} - 10^{19}$ cm^{-3} and 1–15 eV, respectively. For these ranges of plasma conditions the characteristic times of the atomic processes are around 1 ps, which is considerably less than the hydrodynamic time. Therefore, we can assume a sequence of quasi-steady states which are consistent with the instantaneous physical conditions of the plasma and then the time-derivative in the rate equations of the CR model vanishes, obtaining for a given instant τ

$$\sum_{\zeta' j} N_{\zeta' j}(\mathbf{r},\tau) R^{+}_{\zeta' j \to \zeta i} - \sum_{\zeta' j} N_{\zeta i}(\mathbf{r},\tau) R^{-}_{\zeta i \to \zeta' j} = 0. \tag{6}$$

The CR model is implemented in MIXKIP code [50] and the most common atomic processes, both in thermal and photoionized plasmas, are included. They are collisional ionization, three-body recombination, spontaneous decay, collisional excitation and deexcitation, photoionization, spontaneous and induced radiative recombination, autoionization, electron capture, photoexcitation and photodeexcitation. A detailed explanation about how the rates of these atomic processes are determined from their cross sections can be found in [56,57].

The resolution of the RTE and the calculation of the plasma radiative properties are implemented in the RAPCAL code [45], which is coupled to the MIXKIP code. Bound-bound, bound-free and free-free contributions are included in the calculation of the plasma emissivity and absorption coefficient [41]. On the other hand, solving the full time-dependent RTE is necessary to handle radiation flows where very short time scales must be considered but generally not to handle fluid flows where the radiation field at any position in the flow adjust almost instantaneously to changes in the physical conditions. This fact implies that the explicit time variation of the specific intensity in the RTE can be ignored on the characteristic time scales of the flow dynamics, since any characteristic velocity in the flow is considerably smaller than the speed of light. This is the context of this work and, for this reason, the time derivative in Eq.(5) can be dropped. Therefore, the RTE can be written as

$$\frac{\partial I(\mathbf{r},\nu,\mathbf{n})}{\partial s} = j(\mathbf{r},\nu) - \kappa(\mathbf{r},\nu) I(\mathbf{r},\nu,\mathbf{n}), \tag{7}$$

with s the path length traced by the ray passing through the volume $\mathbf{r}$ along the solid angle Ω. The scattering term has not been considered in the RTE since its contribution is irrelevant for the cases analyzed in this work. The formal solution of the last equation is given by

$$I(s,\nu) = I(s_0,\nu) e^{-\tau(s_0,s,\nu)} + \int_{s_0}^{s} j(s',\nu) e^{-\tau(s',s,\nu)} ds', \tag{8}$$

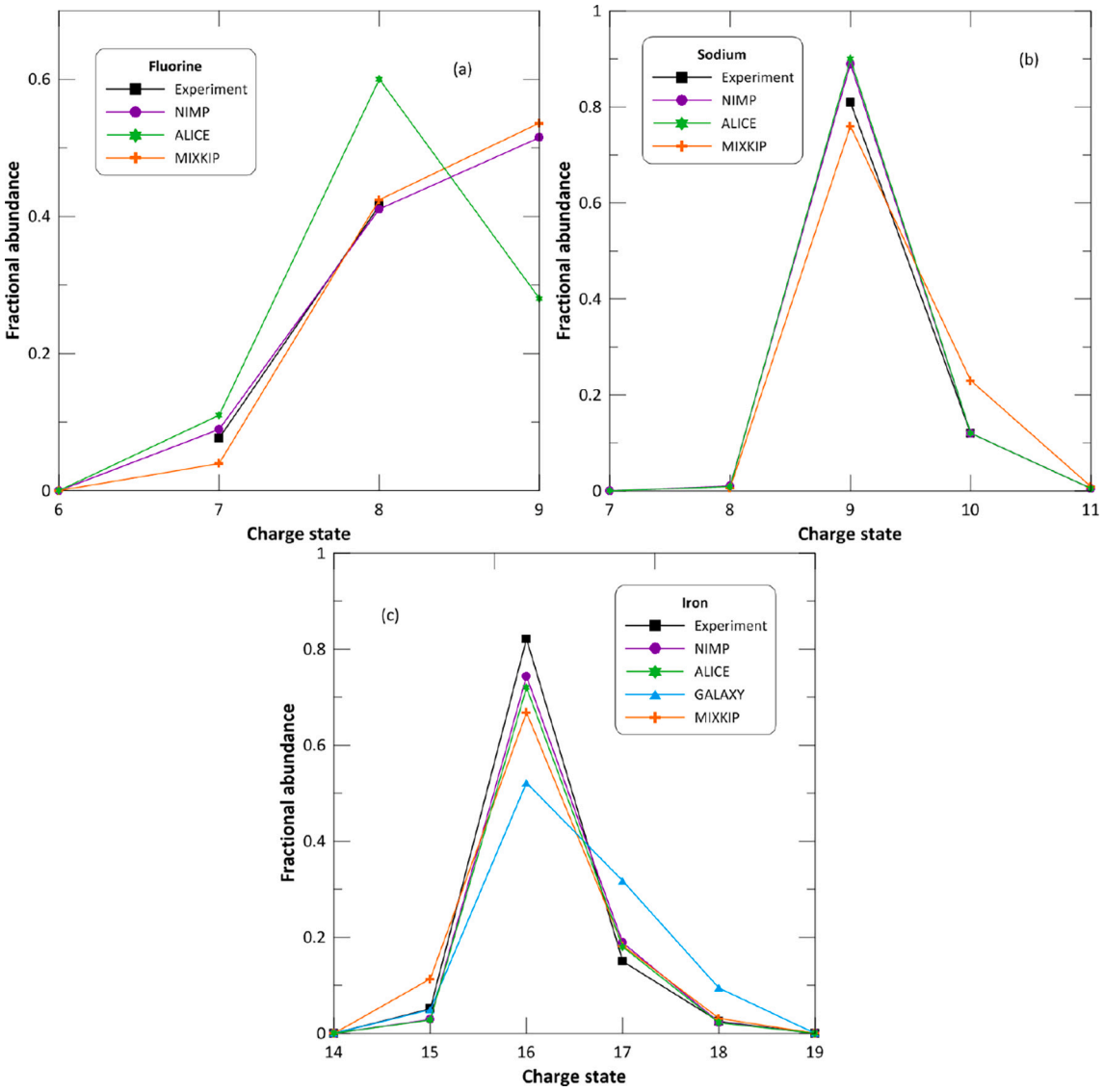

Fig. 2. Comparison of the experimental charge state distributions [70] for a plasma mixture of fluorine (a), sodium (b) and iron (c), with calculations performed by the codes MIXKIP, NIMP [67], ALICE [66] and GALAXY [71]. The conditions of the plasma used in the simulations were an electron temperature of 150 eV, an electron number density of 2×10^{19} cm^{-3} and a Planckian radiation field at a temperature of 165 eV and a dilution factor of 0.01.

where s_0 is the boundary condition and $\tau(s,s',\nu)$ is the monochromatic optical depth at the path length s, which is given by [58].

$$\tau(s^{'},s,\nu) = \int_{s^{'}}^{s} \kappa(s^{''},\nu) ds^{''}. \tag{9}$$

For NLTE optically thick plasmas, since the radiation field couples different cells of the plasma, the rate equations and the RTE of all the layers are solved self-consistently until convergence for the whole plasma is achieved. For photoionized plasmas, as those considered in this work, the specific intensity in Eq.(8) would include the contribution both of the external radiation from the shock front and the radiation emitted by the plasma. In RAPCAL the RTE is solved for 1D and 2D in cartesian geometry.

The atomic structure, oscillator strengths and photoionization cross sections were obtained from the FAC code [57] in which a fully relativistic approach based on the Dirac equation is used. The atomic data were calculated in the detailed configuration accounting approach, including the unresolved transition array (UTA) shifts [59] in the transition energies and a correction to the oscillator strengths due to the configuration interaction within the same non-relativistic configurations. In the evaluation of the line profile, natural, Doppler, electron-impact [60] and UTA [59] broadenings are included. The line-shape function is applied with the Voigt profile including all these broadenings. Complete redistribution hypothesis is assumed for the line profile in the bound-bound transitions. Finally, since the atomic properties are obtained in the context of isolated ion, the effect of the plasma environment on the population of the atomic levels is modeled through the depression of the ionization potential or continuum lowering (CL). The application of the CL can restrict the number of bound states available and, in this work, the formulation developed by Stewart and Pyatt [61] was applied. Furthermore, the transition energies (denoted as E_{th} in Eqs.(2) and (3)) of those collisional and radiative processes that lead to a recombination/ionization of an ion are corrected by the CL.

Multicomponent photoionized plasmas can be also modeled. In this situation, collisional processes that connect ions of different chemical species are not included. However, they are coupled in three ways. First, through the radiation field in the plasma. Secondly, the different species of the multicomponent plasmas are immersed into a common pool of free electrons and, therefore, they are coupled through the electron density since the average ionization of each chemical species has to be

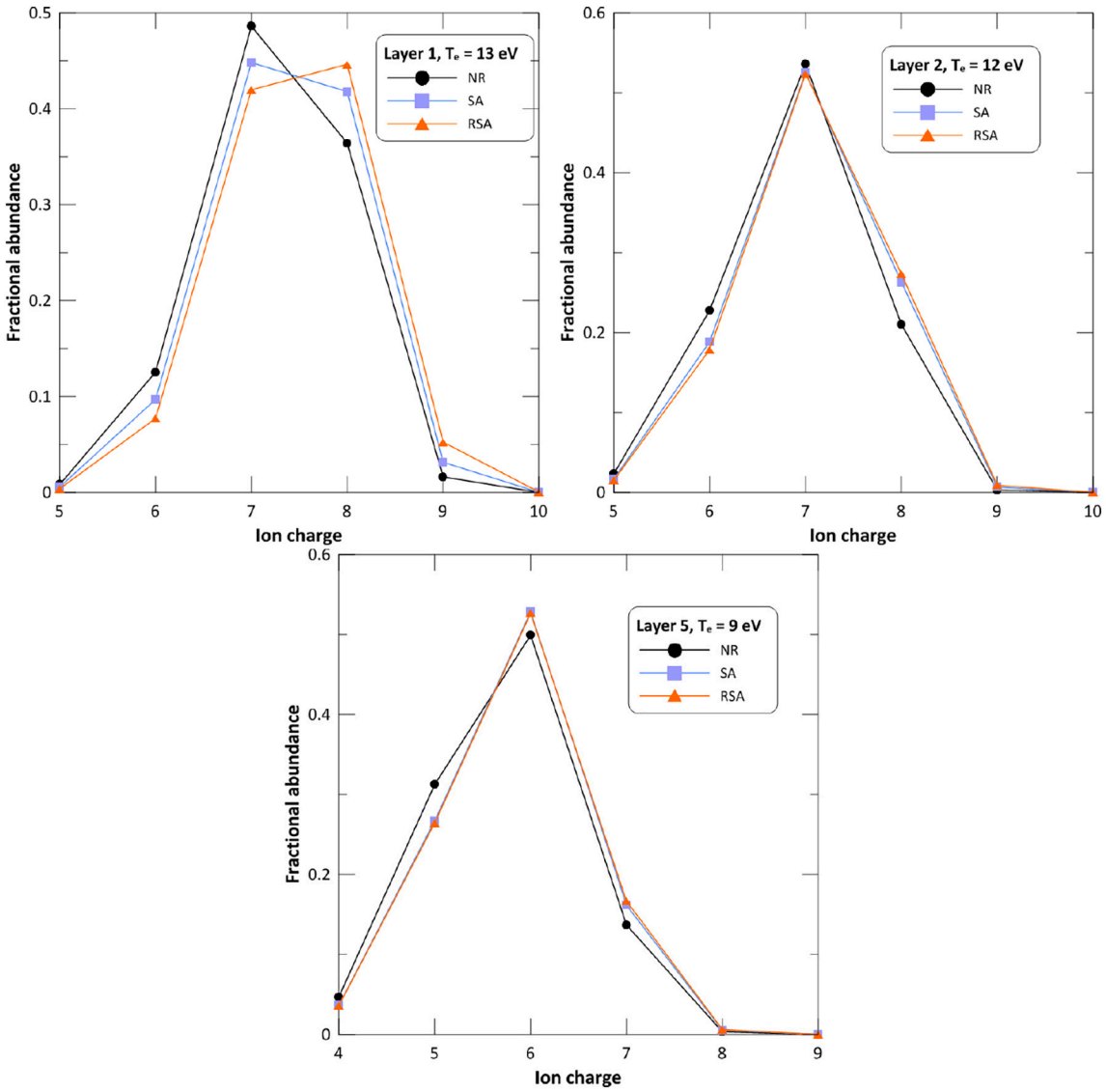

Fig. 3. Comparison of the charge state distributions for three layers of the radiative precursor in the first experiment analyzed.

consistent with same electron density [62]. Finally, they are also coupled through the CL since in the formalism implemented in our CR model this depends on the average ionization of the mixture. Therefore, the rate equations of all chemical species in the plasma must also be solved self-consistently.

The selection of the atomic configurations in the CR models is a key factor but still an open question and largely depends on the problem being addressed. Thus, for example, for plasmas at intermediate densities, ruled by the collision with thermal electrons, the number of double and single excited configurations can be restricted. However, when the plasma is under the influence of high intense radiation fields, atomic configurations with inner shells open might be needed [63]. In this work, we have performed simulations of xenon plasmas for electron temperatures between 1 and 15 eV and mass densities around 10^{-4} gcm^{-3}, which is an intermediate density. For these range of plasma conditions, the ion charge states obtained were between Xe^{0+} and Xe^{10+} and therefore the ionization is not too high. Furthermore, the external radiation field is not so intense as to ionize the innermost shells. According to this, the following configurations were included: (1) ground configuration; (2) single excited configurations from the valence shell, n_v, to shells with $n \leq 10$; (3) doubly excited configurations from the valence shell to shells with $n \leq n_v + 2$; and (4) single excited configurations from shell $n_v - 1$ to shells with $n \leq n_v + 2$. We have checked that this choice is adequate for modeling xenon plasmas in similar plasma conditions [64].

3. Validation of MIXKIP/RAPCAL for photoionized plasmas

The model for photoionized plasmas have been evaluated by comparing its calculations of properties such as average ionization, charge state distribution (CSD) and radiative power loss (which is obtained as the integral in frequencies of the emissivity) with experimental data and numerical simulations from other codes, both for mono- and multi-component plasmas. These comparisons are presented below.

3.1. Nitrogen plasma

The simulations in nitrogen plasmas have been compared with an experiment carried out on the Gekko laser that was used to photoionized a nitrogen gas cell. The ion number density was 1.4×10^{19} cm^{-3} and the radiation field was taken as Planckian with a temperature of 80 eV and an electron temperature between 20 and 30 eV was estimated [65]. The authors obtained the CSD from a spectroscopic diagnostics of an emission spectrum taken at 2.1 ns. In Fig. 1 we compare that CSD with

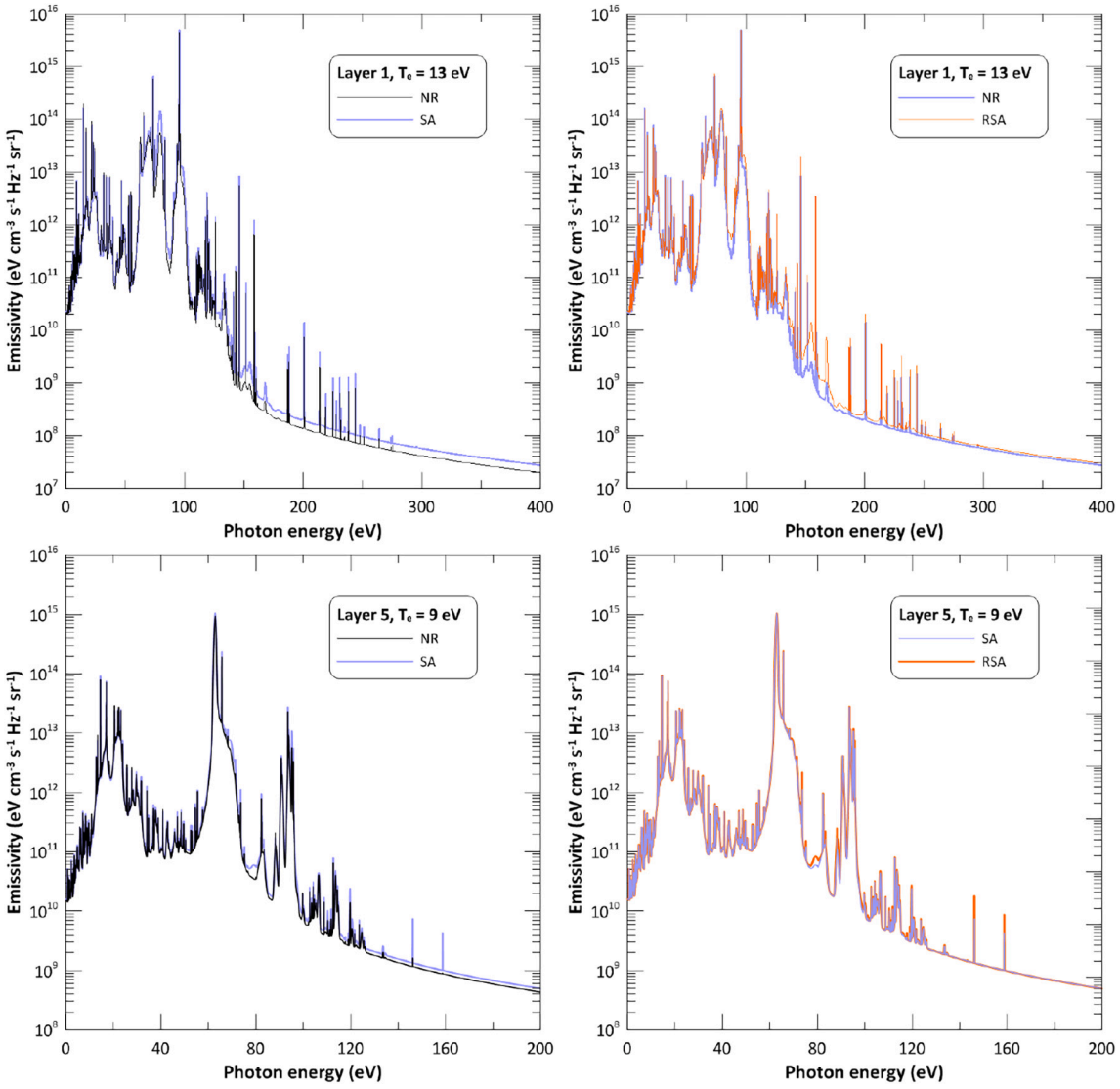

Fig. 4. Comparison of the emissivities calculated with NR, SA and RSA simulations for two layers of the radiative precursor in the first experiment analyzed.

numerical simulations performed with MIXKIP and ALICE [66] and NIMP codes [67]. ALICE and NIMP are CR codes based on a non-relativistic DCA model and on an average atom model, respectively, that include collisional and radiative driven atomic process. We detect from the figure that MIXKIP presents a good agreement with the CSD obtained from the experimental results for the most abundant ions in the plasma, N^{5+} and N^{6+}, showing slight differences for the ions N^{4+} and N^{7+}. On the other hand, the ALICE results were obtained for a temperature of 19 eV, since ALICE predicts that the most abundant ion at the temperature of 20 eV is N^{6+} instead of N^{5+}, which shows the sensitivity of this case with the electron temperature. The NIMP code, which is based on a simple average model, presents a good agreement with the experimental results for the whole CSD. This fact illustrates that, for the calculation of the average ionization, the completeness of the atomic configurations included in the simulations is more critical than accuracy of the atomic data [68]. In this case, configurations with two excited electrons must be included, otherwise the numerical simulations would predict an over-ionized plasma due to low recombination rates [66].

In Table 1 the average ionizations and the CSDs calculated with MIXKIP including or not the external radiation field are compared, in order to show the effect of the photon driven atomic processes. When the external radiation field is not considered in the CR model the CSD is mainly concentrated in two ions, N^{4+} and N^{5+}. The high ionization potential of N^{5+} prevents a greater ionization in the plasma for these conditions of electron temperature and density. On the other hand, when the radiation is considered in the CR simulation the average ionization increases from 4.77 to 5.41, as Table 1 shows. In this case, the radiation driven processes are responsible of populating appreciably the N^{6+} (with a population slightly lower than the population of N^{5+}), overcoming the ionization potential of the ion N^{5+}. However, the higher ionization potential of N^{6+} ion prevents a greater ionization for this external radiation field.

3.2. Neon plasmas

For neon plasmas, we performed calculations of the average ionization and the radiative power loss for electron temperatures of 5 and 40 eV, electron densities of 10^{18} and 10^{19} cm^{-3}, a Planckian radiation field with temperature of 103 eV and a dilution factor of 0.017. These conditions were proposed in the 8th NLTE Code Comparison Workshop [69]. In Table 2 the average ionization and the radiative power loss are listed for these two electron temperatures and densities, compared with calculations from NLTE kinetic codes that participated in that Workshop. From the table, it is detected that the agreement between the results provided by the different codes is better for the case of the higher temperature than for the lower one. This could be due to the fact that He-

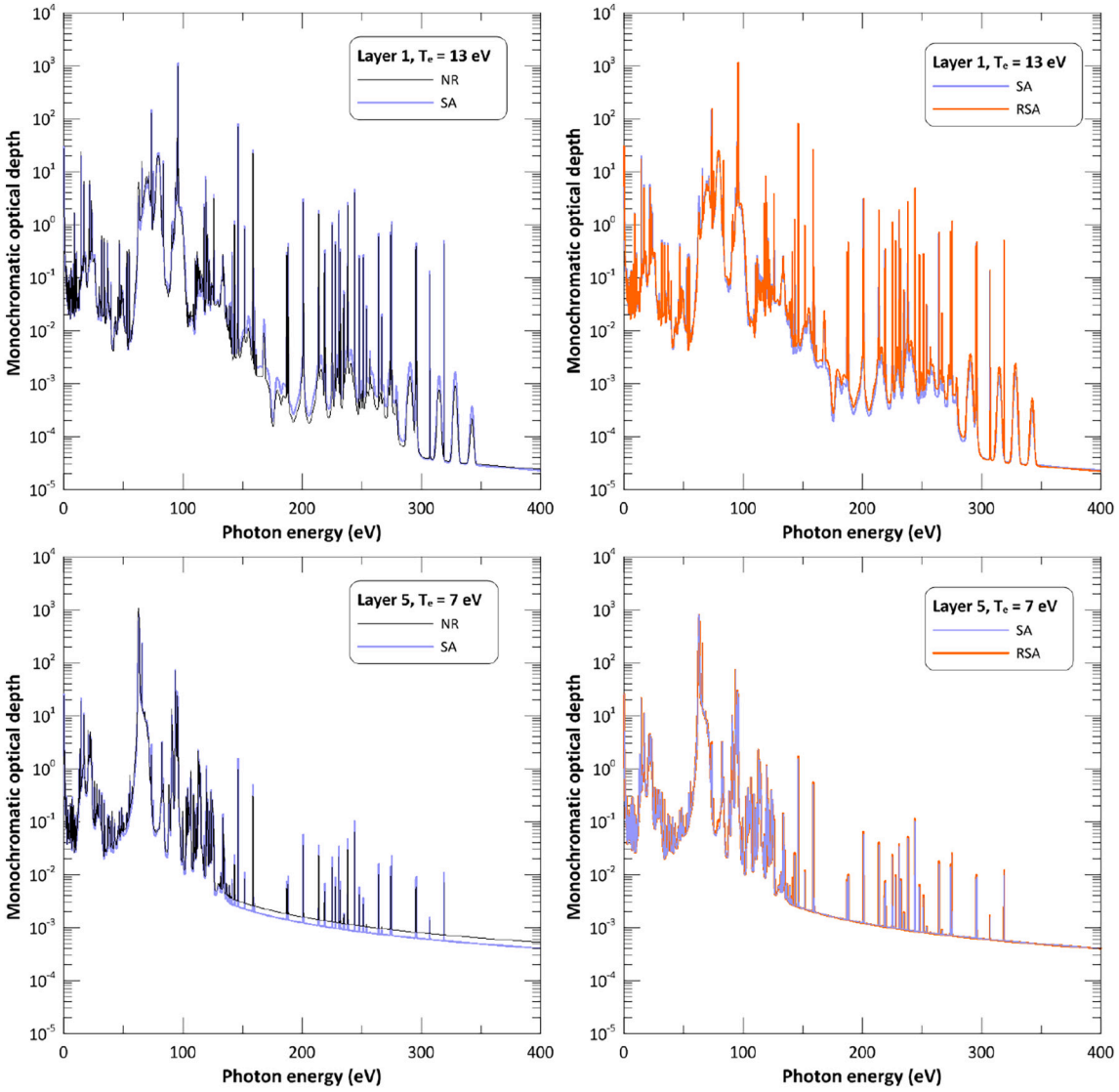

Fig. 5. Comparison of the monochromatic optical depths calculated with NR, SA and RSA simulations for two layers of the radiative precursor in the first experiment analyzed.

like and H-like Ne ions are the most abundant at 40 eV and they have simple atomic structures (He-like is a closed shell ion). In any case, the results obtained with MIXKIP show a good agreement for the four cases, both in the average ionization and in the radiative power loss, with most of the codes compared.

3.3. Plasma mixture

Finally, the CSDs of a plasma mixture have been also compared with an experiment, a thin foil of iron and sodium fluoride that was irradiated by the radiation from a Z pinch [70]. The radiation field was experimentally diagnosed as equivalent to a Planckian with a radiative temperature of 165 eV and a dilution factor of 0.01. The electron density was $n_e = 2.0 \pm 0.7 \times 10^{19}$ cm^{-3} and an electron temperature of 150 eV was found from the analysis of the spectral line shapes.

For the numerical simulations, the atomic level populations were calculated in MIXKIP by iteration over the three elements of the mixture. They are coupled through of the common electron number density and the continuum lowering. Comparisons with the experimental results and also with those obtained using the NIMP and ALICE codes and also, for iron, with the GALAXY code [70] (a CR model based on the average-of-configuration approximation) are illustrated in Fig. 2. The figure shows that MIXKIP provides quite acceptable results for the CSDs of the three elements of the mixture. This agree is only obtained with MIXKIP and NIMP codes since the results provided by the ALICE code do not reproduce the experimental results for fluorine and the CSD obtained with the GALAXY code for iron presents noticeable differences.

4. Results

MIXKIP/RAPCAL has been applied in the analysis of the ion abundances, radiative properties and specific intensities of plasmas in radiative precursors generated by radiative shocks launched in xenon in two kinds of laboratory experiments. In the first one, the shock is launched in a tube by driving with the laser a solid piston into a xenon gas cell. This kind of experiments is commonly used to recreate accretion shocks. In the second type, which is appropriate to recreate radiative shocks in supernova remnants, the laser energy is deposited directly into a cluster of xenon. A brief description of the experiments is included before presenting the results.

Three types of collisional-radiative models have been used in the numerical simulations of the plasmas properties of the radiative precursors in both experiments. In the first one, denoted as NR, the radiation induced processes were not included. In the second type, the

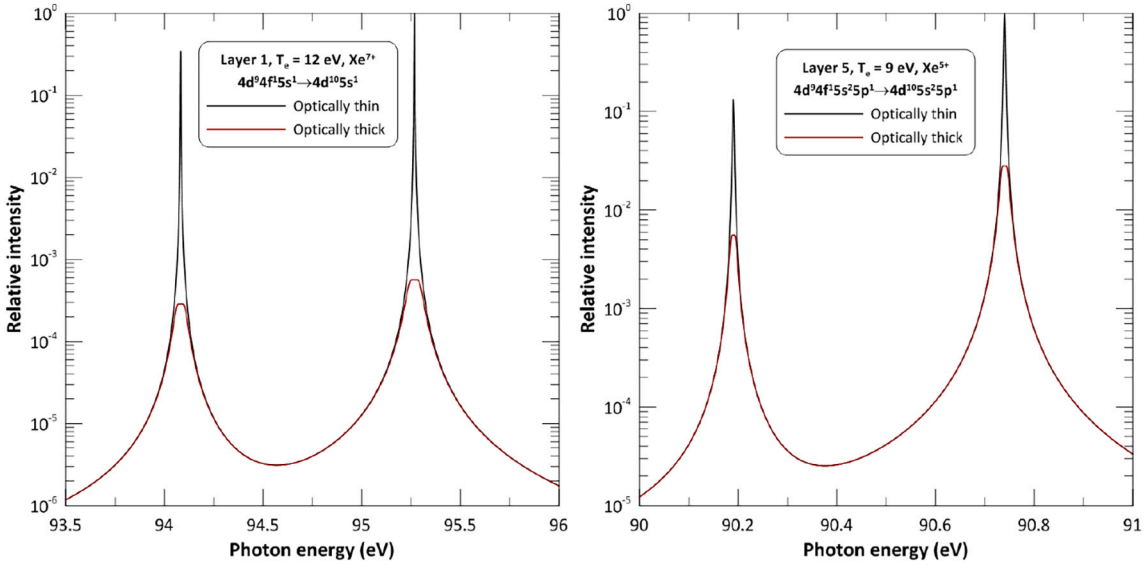

Fig. 6. Comparison of the relative intensities of two line transitions of Xe^{7+} and Xe^{5+} for layers 1 and 5, respectively, in the first experiment analyzed, calculated with NR model assuming the plasma as optically thin or thick for the line transport in the layer.

radiative atomic processes induced by plasma self-absorption were considered and it has been denoted as SA. Thus, we can analyze the effect of the plasma self-absorption on the atomic level populations and absorption and emission coefficients. Finally, the radiative processes induced by both the external radiation field (to model the photoionized plasma) and the plasma self-absorption were included in the third type of simulation, denoted as RSA. Furthermore, for the three types of numerical simulations, the influence of the plasma self-absorption on the specific intensities in the radiative transport has been also analyzed.

4.1. Radiative shock launched in a tube

The first experiment considered [12] was performed at the Prague Asterix Laser System facility. The setup consisted of a target which is a channel of parallel pipe shape, whose length is 4 mm, filled with xenon at 0.1 bar (mass density of 5.4×10^{-4} gcm^{-3}). The target is closed at both ends by two foils made of plastic and coated with gold. They act as pistons to drive the shock into the target. The shock wave was driven by focusing a laser beam (133 J, $\lambda = 438$ nm) onto the left piston. The laser pulse is long ($\sim$ ns) which implies a continuous injection to the shock and the creation of a stationary structure [72]. The velocity of the shock was estimated using visible interferometry diagnostic obtaining 50 ± 3 km/s. Using the lagrangian code HELIOS [73], 1D radiation-hydrodynamics calculations in the direction of the shock propagation were performed [12]. The plasma conditions thus obtained have been used in the numerical simulations carried out in this work as described below.

HELIOS calculations predicted a temperature of around 16 eV and a mass density of 0.011 gcm^{-3}, what corresponds to an electron density of 6.7×10^{20} cm^{-3} for the shock. For these conditions, the plasma in the shocked medium can be assumed in LTE [74]. Therefore, we have modeled the radiation coming from the shock front as Planckian with a radiation temperature of 16 eV. With respect to the radiative precursor, an extension of 0.165 cm and temperatures ranged between 13 and 7 eV were obtained in the radiation-hydrodynamics calculations at 10 ns. For the CR simulations, we have divided the precursor extension in the direction of the shock propagation into 7 uniform layers with electron temperatures from 13 to 7 eV and with a mass density of 5.4×10^{-4} gcm^{-3}. Therefore, the atomic kinetics and radiation transfer in the radiative precursor are solved in 1D. The range of electron densities for the radiative precursor obtained from NR, SA and RSA simulations are quite similar, since the ions involved are the same, and are ranged from 1.9×10^{19} cm^{-3} to 1.3×10^{19} cm^{-3} which are in good agreement with those obtained in the HELIOS simulations, ranged between $2.0 - 1.8 \times 10^{19}$ cm^{-3}.

The comparison of the CSDs for three layers obtained with the NR, SA and RSA simulations is depicted in Fig. 3. It is observed that the main ions involved in the two first layers are the same, Xe^{6+}–Xe^{9+}, since their temperatures are close. In layer 1 it is detected that the most abundant ion is Xe^{7+} for the NR simulation. An increase in the ionization is observed when the plasma self-absorption is included (SA model), although the most abundant ion remains the same. When the radiation from the shock front is also included (RSA model), the increase of the ionization becomes more noticeable, now being Xe^{8+} the most abundant ion. However, it is obtained that in layer 2 (and the following layers) the results provided by SA and RSA models are very similar which indicates that the effect of the external radiation field is almost negligible and the small increase in ionization seen in the figure is mainly due to self-absorption in the plasma. We have verified that the radiation emitted by the shock front is absorbed almost entirely by the neighboring region of the precursor due to the value of its mass density. Thus, the same simulations were performed decreasing the density to 10^{-4} gcm^{-3}, obtaining that the effects of the external radiation field would be noticeable even in the final region of the precursor (which corresponds to layer 7 in our model). Therefore, for this experiment, once the radiative precursor is generated by the radiation from the shock front, the influence of that radiation on the atomic level populations is limited to the region closest to the front (layer 1).

The changes produced in atomic level populations due to radiation-induced atomic processes are propagated to the emission and absorption coefficients. The comparisons of the emissivities obtained with the three types of simulations for layers 1 and 5 are displayed in Fig. 4. According to Fig. 3, the ions that contribute the most to the emissivity are the same in NR, SA and SRA calculations, Xe^{5+}–Xe^{9+} and Xe^{4+}–Xe^{8+} for layers 1 and 5, respectively, and this fact explains that the structures obtained in the emissivities in the three simulations are the same. The discrepancies are obtained in the values of the emissivity due to the differences in the ion populations. Fig. 3 showed that the main effect of radiation (both the external and the emitted by the plasma) is to increase the plasma ionization, being this effect more important in layer 1 than in layer 5. This is also clearly observed in Fig. 4 which shows that the differences in the emissivities between the three simulations are more noticeable in layer 1

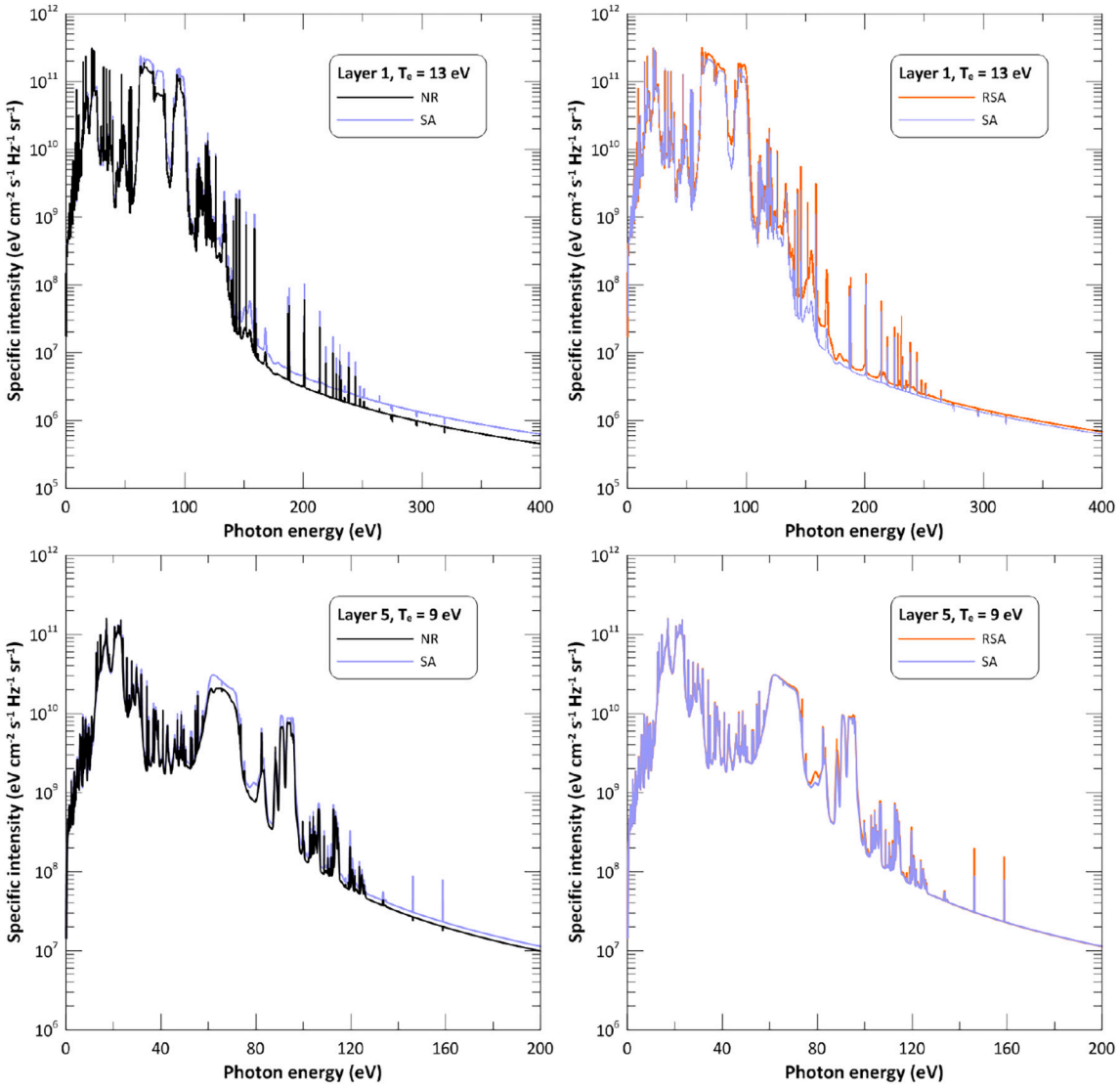

Fig. 7. Comparison of the specific intensities calculated with NR, SA and RSA simulations for two layers of the radiative precursor in the first experiment analyzed.

than in layer 5. In the former layer we detect that for the region of low photon energies (less than 50 eV and mainly between 20 and 30 eV) the NR simulation provides slightly higher values of the emissivity of some lines than the SA and RSA calculations. These are line transitions of the ions Xe^{6+} and Xe^{7+} which contribute mainly in this energy region of the spectrum. In contrast, the region of photon energies greater than 60 eV, where the contributions of the ions Xe^{8+} and Xe^{9+} are more relevant, the values of the emissivities provided by the SA and RSA simulations are higher than those obtained with NR. Contributing to these increases, in addition to a greater abundance of these ions, is the fact that the populations of the excited levels are more populated than in the NR simulation due to the photoexcitation induced by radiation. We have found that the relative populations of excited states, with respect to that of the ground configuration, can be doubled in the SRA simulation. In layer 1, since the external radiation produces a higher ionization than the plasma self-absorption, differences are also detected in the emissivities calculated with SA and RSA simulations. The behavior of these differences with the photon energy is similar to that obtained between the NR and SA simulations.

On the other hand, these differences are not obtained in layer 5, the SA and RSA emissivities being rather similar. This result was expected according to the agreement between the CSDs depicted in Fig. 3. Therefore, in this layer, the discrepancies in the emissivity with respect to the NR simulations are mainly due to the effect of the plasma self-absorption on the atomic level populations. In general, the values of the emissivity provided by the NR simulation are smaller than those obtained with SA, although the abundance of Xe^{5+} is larger for the NR simulation. This is due to in the range of photon energies lower than 60 eV, where Xe^{5+} contributes, the contributions to the emissivity of Xe^{6+} and Xe^{7+}, whose populations are larger in the SA simulation, are also present producing the increase of the SA emissivity with respect to NR simulation.

Similar results are obtained for the absorption coefficient, as Fig. 5 shows. In that figure the monochromatic optical depths of layers 1 and 5, calculated with the three simulations, are represented. This figure, in addition to showing the differences in the absorption coefficient due to changes in plasma populations, allows us to analyze whether self-absorption will influence on the intensity when the line is transported in the layer. In layer 1 the optical depth is greater than or close to 1 in many ranges of photon energies and this occurs in the three simulations. Therefore, even if the effect of self-absorption was not included in the CR model (as in the case of the NR simulation), many lines are optically thick and the self-absorption must be included in their transport. This also occurs in layer 5 for line transitions in the range of photon energies lower than 150 eV. This fact is illustrated in Fig. 6, which shows the relative intensities of two line transitions of Xe^{7+} and Xe^{5+} for layers 1

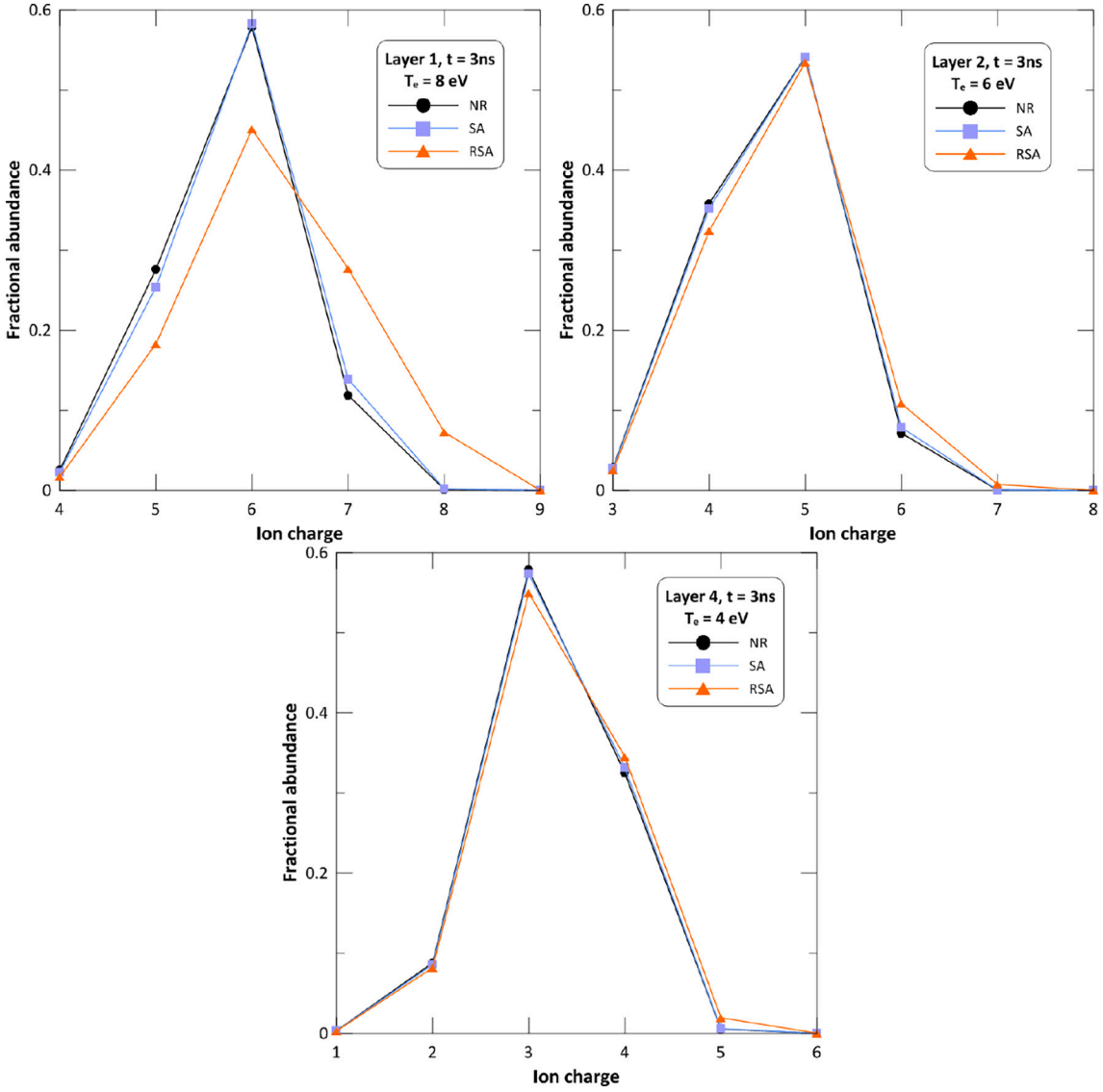

Fig. 8. Comparison of the charge state distributions at 3 ns for three layers of the radiative precursor in the second experiment analyzed.

and 5, respectively, obtained with the NR collisional-radiative model assuming that the plasma is optically thick or thin for these lines. Since the calculations were done with the NR model, the influence of the self-absorption on the level populations is not included in this comparison. Therefore, the differences between both calculation of the line intensities are only due to plasma self-absorption effects on the line transport through the layer. The optical depths for these transitions are greater than 1 and the figure shows a strong absorption at the lines center, decreasing in two or three orders of magnitude, depending of the layer. Therefore, in the following, the specific intensities of the layers calculated with the three types of CR models will include the plasma self-absorption in the radiative transport of the lines. Thus, the differences between their intensities will be only due to the changes in the plasma atomic level populations.

The comparison of the specific intensities calculated with the three CR models for layers 1 and 4 is illustrated in Fig. 7. Since the ions that contribute are the same for the three simulations, Xe^{5+}–Xe^{9+} and Xe^{4+}–Xe^{8+} for layers 1 and 5, respectively, the structures observed in the intensities obtained with the three models are the same. However, some discrepancies are detected in the values of the line intensities due to the differences in the ion populations, which is expected according to the results already obtained when analyzing the emissivities and the monochromatic optical depths (see Figs. 5 and 6). In layer 1, for the region of low photon energies (less than 60 eV), where the ions that must contribute are Xe^{6+} and Xe^{7+}, the NR simulation provides slightly higher values of intensity than the SA and RSA calculations. In contrast, in the region of photon energies greater than 60 eV, where the contributions of the ions Xe^{8+} and Xe^{9+} are more relevant, the values of the intensity provided by the SA and RSA models are sensibly higher, especially in the latter case. Contributing to this increase, in addition to a greater abundance of these ions, is the fact that the populations of the excited levels of the ions are also greater than in the NR simulation due to photoexcitation by radiation. This is most noticeable in the RSA model, which shows the high influence of the radiation field coming from the shock front. As said before, we have found that the relative population of excited states, with respect to that of the ground configuration, can be even double when the external radiation is considered, increasing the emissivity from those states. In layer 5, a similar behavior to layer 1 is obtained, but the differences are now significantly less. They are mainly due to the influence of the plasma self-absorption on the atomic level populations and not to the external radiation field which is mostly absorbed in layer 1, as anticipated when commenting on ion populations. Finally, the impact of self-absorption on the line transport can be observed by comparing the emissivities with the specific intensities

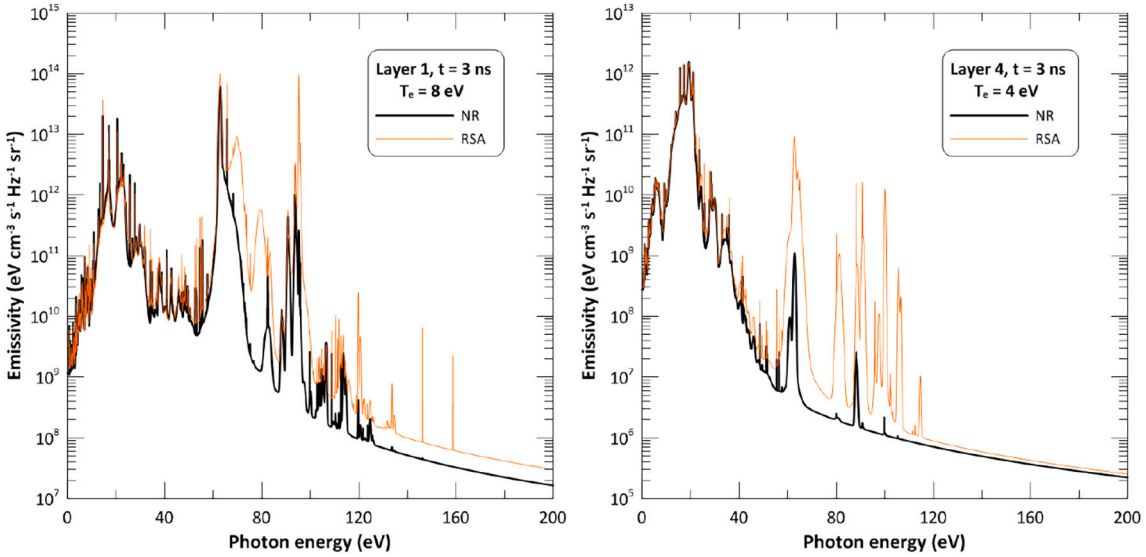

Fig. 9. Comparison of the emissivities calculated with NR and RSA collisional-radiative models of layers 1 and 4 of the radiative precursor at 3 ns in the second experiment analyzed.

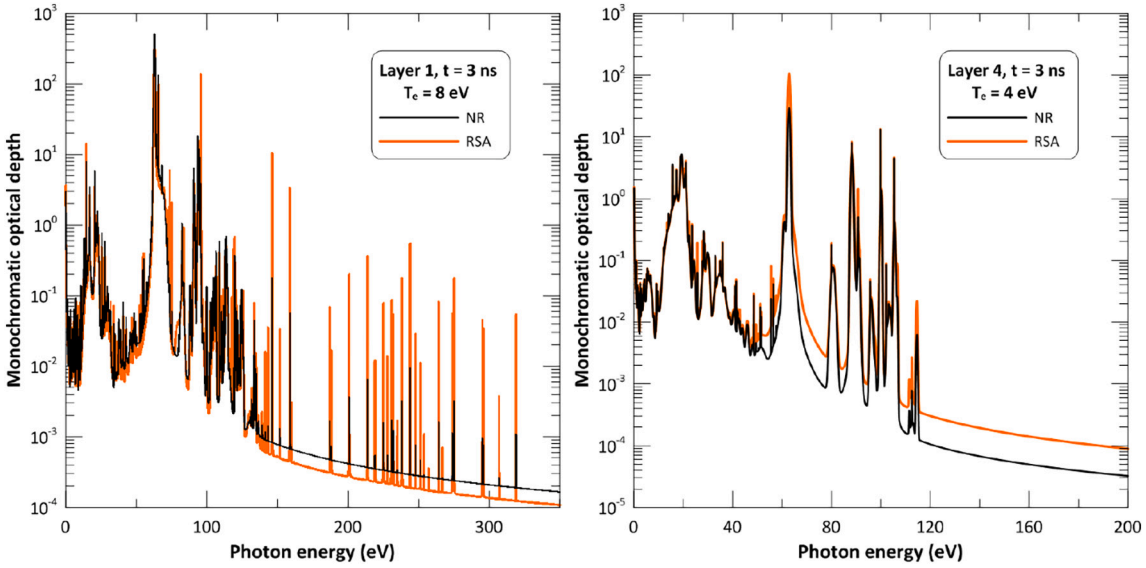

Fig. 10. Comparison of the monochromatic optical depths calculated with NR and RSA collisional-radiative models of layers 1 and 4 of the radiative precursor at 3 ns in the second experiment analyzed.

(Figs. 4 and 7). As previously shown, in the line transport the emission intensity is reduced by self-absorption, its effect being more important in some regions of photon energy than in others, for example, in layer 1 between 50 and 100 eV and around 150 eV.

4.2. Radiative shock launched in a cluster

The second experiment analyzed was conducted using the THOR laser facility at the University of Texas [17]. In this case, the shock was produced after the laser energy was deposited directly into a gas of xenon clusters. Clustered gases present an extremely efficient absorption of the laser energy creating a hot, high energy density plasma. The plasma subsequently explodes into the xenon gas forming a cylindrical radiative blast wave [75], which is an expanding radiative shock that is in the process of sweeping up the material that is ahead of the shock. In this experiment, the gas of xenon cluster was irradiated with a laser energy around 400 mJ at average gas density of 1.6×10^{-4} gcm^{-3}, which is the density of the radiative precursor generated ahead of the front shock. The pulse duration was short (~ps) and, in this case, the temperature of the shock decreased with time due the energy loss by radiation. The blast waves formed were characterized using time-resolved transverse interferometric and Schlieren image. In this way, the electron density profiles in the radial direction (which is the direction of the shock propagation) could be obtained at several times.

We have performed the analysis of this experiment at 3 ns and 21 ns after the shock was launched. Using the experimental mass density and radial electron density profile, the radial electron temperature profiles for both the shocked medium and the radiative precursor were obtained using a CR model [76]. These radial temperature profiles have been used in this work. Experimental data provides a shocked shell compression equals to 2, which implies a mass density of 3.2×10^{-4} gcm^{-3}. For this mass density and for the temperatures reached in the shocked shell (lower than 20 eV), the plasma is in NLTE and, therefore, its radiation field cannot be modeled with a Planckian function, as was done in the

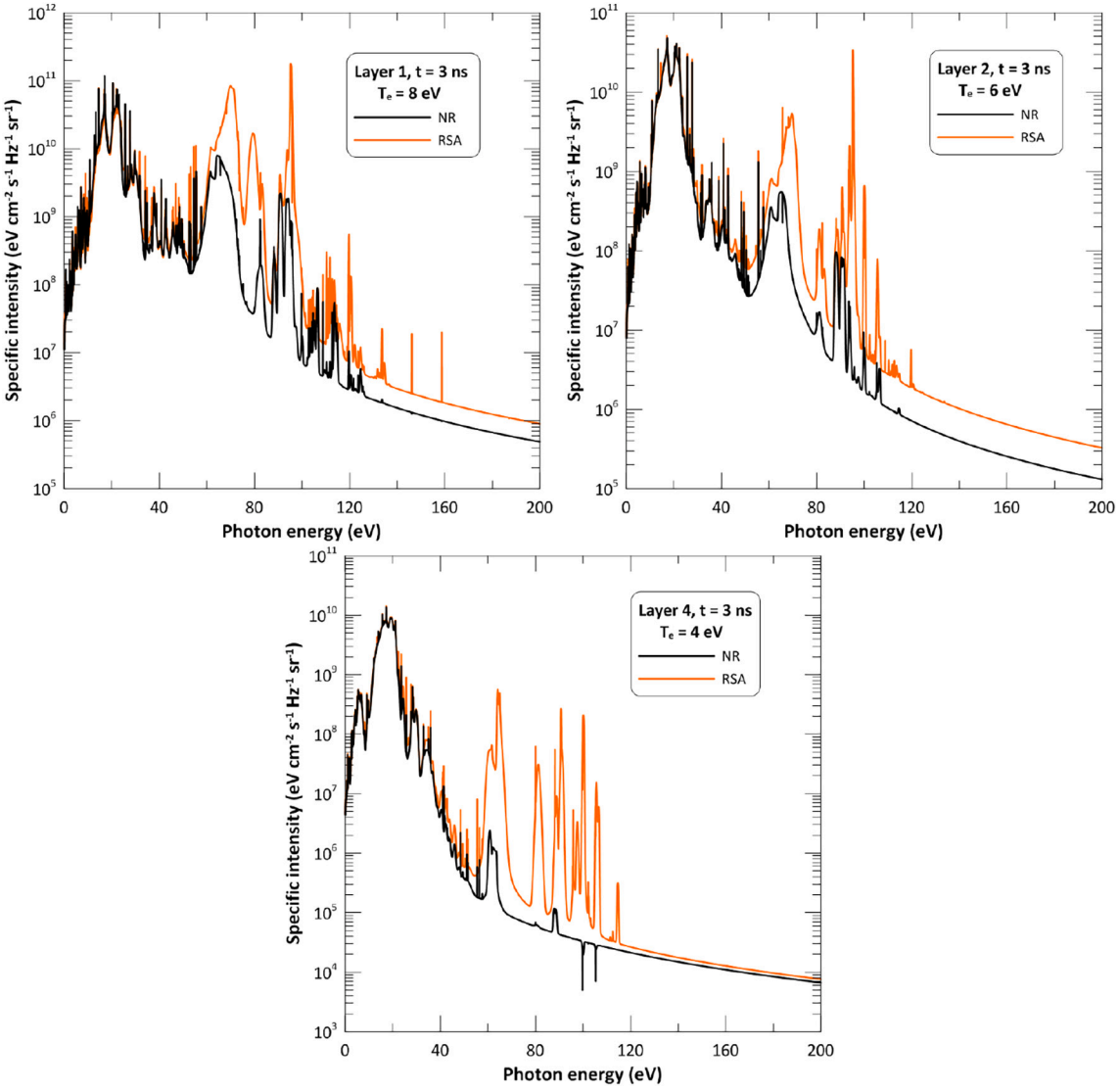

Fig. 11. Comparison of the specific intensities for three layers of the radiative precursor at 3 ns in the second experiment analyzed.

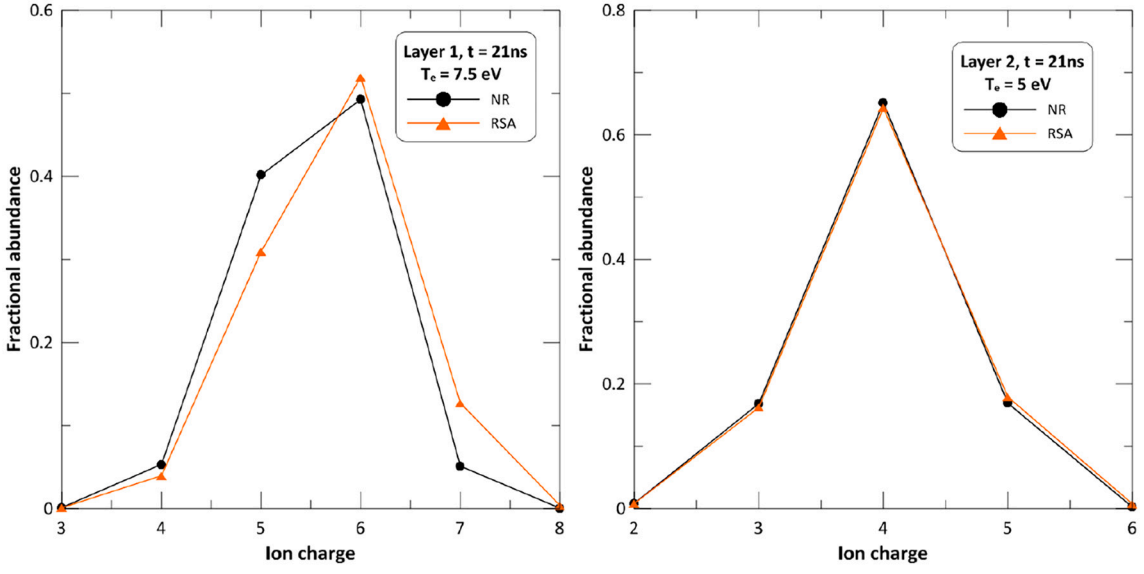

Fig. 12. Comparison of the charge state distributions at 21 ns for two layers of the radiative precursor in the second experiment analyzed.

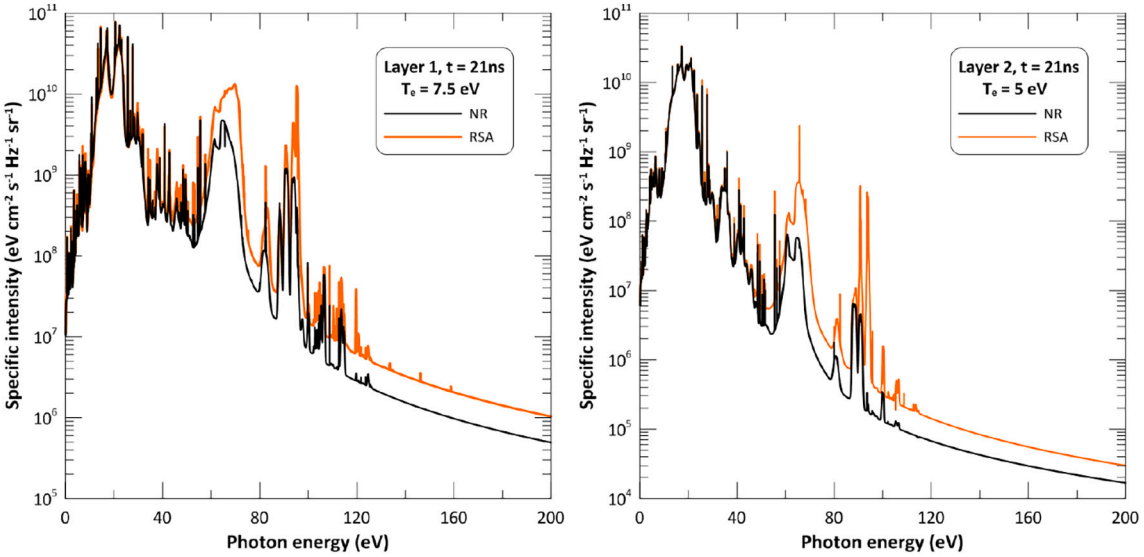

Fig. 13. Comparison of the specific intensities for two layers of the radiative precursor at 21 ns in the second experiment analyzed.

previous experiment. In this case, we have calculated the radiation emitted by the shock front with the CR model. For the numerical simulations of the plasma in the radiative precursor, this was divided, in the radial direction, into a non-uniform spatial grid of 7 layers with the same mass density but different electron temperature.

At $t = 3$ ns, the temperature of the shock front was 15 eV and the length of the radiative precursor was 0.11 cm with temperatures ranged between 8 and 1 eV. As expected, the radiation coming from the shock leads to an increase in ionization that is more noticeable in the regions closer to the front (layer 1), as Fig. 8 shows. However, unlike the first experiment analyzed, it is observed that the impact of the plasma self-absorption on the ion populations is small in layer 1 and almost negligible in the other layers. This result is due to the lower density of the precursor in this second experiment. Therefore, in this case, we have focused the analysis on the influence of the radiation coming from the shock front. However, although self-absorption has a negligible contribution on the ion abundances, its impact on the line intensities in the line transport through the layer is relevant and must be included, as will be shown below.

The comparisons of the emissivities and monochromatic optical depths of layers 1 and 4, calculated with NR and RSA collisional-radiative models, are displayed in Figs. 9 and 10. The noticeable differences in these properties between both models are detected in the figures. This is due to the influence of the external radiation field on the radiative properties, being more important in layer 1 than in layer 4. This result was expected since it also occurred in the ion abundances. In layer 1, both models predict transitions for the photon energies greater than 160 eV that are detected in the optical depth but not in the emissivity. These are transitions from the ground configuration to excited configurations of Xe^{8+}, the absorption obtained with the RSA model being more important than with the NR model, since the abundance predicted by the former is greater. However, the populations of the excited states of this ion are considerably small and therefore transitions in that range of photon energies are not detected in the emissivity. On the other hand, the NR model predicts in layer 4 structures in the monochromatic optical depth that are not detected in the emissivity for the photon energy range 80–120 eV. These correspond to transitions from doubly excited levels of Xe^{4+} and Xe^{5+} to the ground configuration and the two first excited levels. However they are obtained both in the emissivity and the optical depth calculated with the RSA model. This result shows that the photoexcitation process, responsible for populating those excited levels, plays a pivotal role in this experiment, producing significant differences even when the discrepancies in the ion populations between the RSA and NR simulations are small, as occurs in layer 4.

Figure 10 also shows that many transitions for photon energies lower than 100 eV have an optical depth greater than or close to one in both CR models. Therefore, the plasma self-absorption must be included in the calculation of the specific intensity transported through the layer in both RSA and NR models. The comparisons of the specific intensities for layers 1,2 and 4 are illustrated in Fig. 11. The differences between them are only due to the plasma atomic level populations and those are more noticeable for photon energies greater than 60 eV, which is expected since the differences in the emissivities were also more relevant in that range of photon energies, as Fig. 9 showed. The discrepancies between RSA and NR calculations of the specific intensities are greater in this experiment than in the previous one. In this second experiment the electron density is lower than in the first one analyzed, between 6×10^{18} and 10^{18} cm^{-3}. These lower electron densities lead to a decrease in the collisional excitation rate. Therefore, photoexcitation process becomes more relevant to populate the excited levels, which would explain these greater differences with respect to the NR simulations. The effect of the plasma self-absorption on the emission spectra can be observed in those range of photon energies in which the monochromatic optical depths were greater than or close to one by comparing the emissivities (Fig. 9) and the specific intensities (Fig. 11).

At $t = 21$ ns, the temperature of the shock had decreased to 9 eV, the length of the radiative precursor was 0.09 cm with temperatures ranged between 7.5 and 1 eV. At this time, the intensity of the radiation emitted by the shock front is lower and so is its effect on the properties of the radiative precursor. This is illustrated in Fig. 12, where we observe that the influence on the ion populations is less than at earlier times. However, differences in the specific intensities provided by the NR and RSA models are still observed, although they are smaller than at 3 ns, as Fig. 13 shows. The ion abundances obtained in layer 2 with both models are very similar. However, the values of the intensity provided by the RSA model are greater than those of the NR model which is due to the influence of the photoexcitation process induced by the shock front radiation on the population of the excited levels. In layer 1, this effect is also present but the fact that the discrepancies in the ion abundances are greater than in cell 2 also contributes to the increase the differences observed between both simulations. The total duration of this experiment was around 80 ns. As time passes, the intensity of the shock radiation decreases and the results of the RSA and NR models will tend to converge.

5. Conclusions

In this work we have performed a numerical analysis of the influence of the radiation induced atomic processes on the atomic kinetics, radiative properties and emission spectra for a type of photoionized plasmas such as those found in radiative precursors generated in experiments of laser-produced radiative shocks. Two experiments have been studied, in which the radiative shocks were launched in xenon, that recreate accretion shocks and supernova remnants, respectively, being the mass density in the second experiment around five times lower than in the first one. For the numerical simulations, we have used a large-scale collisional-radiative and radiative transfer coupled models in which a complete set of atomic configurations of xenon was implemented. In the calculation of the photon induced atomic processes in the rate equations, the radiation included both the external radiation field coming from the shock front and the radiation emitted by the plasma. These processes influence the ionization balance increasing the ionization relative to the optically thin situation. Furthermore, for a given ion, the photoexcitation induced by the radiation can increase the relative populations of excited states, with respect to that of the ground configuration. These two factors imply changes in the plasma properties that may become rather relevant. Thus, in the first experiment, we obtained that the external radiation field was mainly absorbed in the region of the radiative precursor closer to the shock front, producing significant changes in the ion abundances and radiative properties. For regions farther from the front, the influence of the external radiation was negligible and the differences were due to the plasma self-absorption. In the second experiment the mass density was lower and as a consequence the external radiation was not only absorbed in regions close to the front, but produces changes in the entire radiative precursor and, in addition, the influence of the self-absorption on the atomic kinetics is considerably less than in the first experiment. In NLTE optically thick plasmas, self-absorption influences on the emission spectra through both the atomic level populations and line transport. In both experiments, the analysis of the monochromatic optical depths showed that many lines were optically thick and they were partially or strongly absorbed in the line transport. Therefore, even when the impact of self-absorption on atomic kinetics was negligible, it had to be included in the numerical simulation of the emission spectra.

Declaration of Competing Interest

The authors declare that they have no known competing financial interests or personal relationships that could have appeared to influence the work reported in this paper.

Data availability

Data will be made available on request.

Acknowledgments

This work has been supported by the Spanish Government through the Project PID2019-110678GB-I00.

References

[1] B.A. Remington, P.R. Drake, D.D. Ryutov, Experimental astrophysics with high power lasers and z pinches, Rev. Mod. Phys. 78 (2014) 755–807, https://doi.org/10.1103/RevModPhys.78.755.
[2] D.D. Ryutov, R.P. Drake, J. Kane, R. B. A, W.M. Wood-Vasey, Similarity criteria for the laboratory simulation of supernova hydrodynamics, Astrophys. J. 518 (1999) 821–832, https://doi.org/10.1086/307293.
[3] D.D. Ryutov, R.P. Drake, R. B. A, Criteria for scaled laboratory simulations of astrophysical MHD phenomena, Astrophys. J. Suppl. Ser. 127 (2000) 465–468, https://doi.org/10.1086/313320.
[4] J.I. Castor, Astrophysical radiation dynamics: the prospects for scaling, Astrophys. Spac. Sci. 307 (2000) 207–211, https://doi.org/10.1086/313320.
[5] E. Falize, S. Bouquet, C. Michault, Scaling laws for radiating fluids: the pillar of laboratory astrophysics, Astrophys. Spac. Sci. 322 (2009) 107–111, https://doi.org/10.1007/s10509-009-9983-z.
[6] S. Bouquet, E. Falize, C. Michault, C.D. Gregory, B. Loupias, T. Vinci, M. Koenig, From lasers to the universe: scaling laws in laboratory astrophysics, High Energy Density Phys. 6 (2010) 368–380, https://doi.org/10.1016/j.hedp.2010.03.001.
[7] B. Commercon, E. Audit, J.P. Chieze, Physical and radiative properties of the first-core accretion shock, Astron. Astrophys. 530 (2011) A13, https://doi.org/10.1051/0004-6361/201016213.
[8] J.M. Blondin, E.B. Wright, K.J. Borkowski, S.P. Reynolds, Transition to the radiative phase in supernova remnants, Astrophys. J. 500 (1998) 324–354, https://doi.org/10.1086/305708.
[9] E. Huguet, J. P. J, Radiative shocks in atomic and molecular stellar-like atmospheres.8. a self-consistent comprehensive model, Astron. Astrophys. 324 (1997) 1046–1058.
[10] A.C. Raga, G. Mellema, S.J. Arthur, L. Binette, P. Ferruit, W. Steffen, 3d transfer of the diffuse ionizing radiation in ISM flows and the preionization of a Herbig-Haro working surface, Rev. Mex. Astron. Astrophys. 35 (1999) 123–133.
[11] Y.B. Zel'dovich, Y.P. Raizer, Physics of Shock Waves and High-Temperature Hydrodynamic Phenomena, Dover Publications Inc., New York, 2002.
[12] R.L. Singh, C. Stehle, F. Suzuki-Vidal, M. Kozlova, J. Larour, U. Chaulagain, T. Clayson, R. Rodriguez, J.M. Gil, J. Nejdl, M. Krus, J. Dostal, R. Dudzak, P. Barroso, O. Acef, M. Cotelo, P. Velarde, Experimental study of the interaction of two laser-driven radiative shocks at the PALS laser, High Energy Density Phys. 23 (2017) 20–30, https://doi.org/10.1016/j.hedp.2017.03.001.
[13] R.P. Drake, Y. Davidson, Y. Horie, High-Energy-Density Physics: Fundamentals, Inertial Fusion and Experimental Astrophysics, Springer, New York, 2006.
[14] K. Keilty, E. Liang, T. Ditmire, B. Remington, K. Shigemori, A. Rubenchick, Modeling of laser-generated radiative blast waves, Astrophys. J. 538 (2000) 645–652, https://doi.org/10.1086/309164.
[15] S. Bouquet, C. Stehle, M. Koenig, J.P. Chieze, A. Benuzzi-Mounaix, D. Batani, S. Leygnac, X. Fleury, H. Merdji, C. Michaut, F. Thais, N. Grandjouan, T. Hall, E. Henry, V. Malka, J.P.J. Lafon, Observation of laser driven supercritical radiative shock precursors, Phys. Rev. Lett. 22 (2004), 056501, https://doi.org/10.1103/PhysRevLett.92.225001.
[16] J.F. Hansen, M.J. Edwards, D.H. Froula, G. Gregori, A.D. Edens, T. Ditmire, Secondary shock formation in xenon-nitrogen mixtures, Phys. Plasmas 13 (2006), 022105, https://doi.org/10.1063/1.2359283.
[17] J. Osterhoff, D.R. Symes, A.D. Edens, A.S. Moore, E. Hellewell, T. Ditmire, Radiative shell thinning in intense laser-driven blast waves, New J. Phys. 11 (2009), 023022, https://doi.org/10.1088/1367-2630/11/2/023022.
[18] F. Doss, R.P. Drake, C. Kuranz, Repeatability in radiative shock tube experiments, High Energy Density Phys. 6 (2010) 157–161, https://doi.org/10.1016/j.hedp.2009.12.007.
[19] A.D. Edens, R.G. Adams, P. Rambo, L. Ruggles, I.C. Smith, J.L. Porter, T. Ditmire, Study of high Mach number laser driven blast waves in gases, Phys. Plasmas 17 (2010), 112104, https://doi.org/10.1063/1.3491411.
[20] C. Stehle, M. Kozlova, J. Larour, J. Nedjl, N. Champion, P. Barroso, F. Suzuki-Vidal, O. Acef, P.A. Delattre, J. Dostal, M. Krus, J.P. Chieze, New probing techniques of radiative shocks, Opt. Commun. 285 (2012) 64–69, https://doi.org/10.1016/j.optcom.2011.09.008.
[21] U. Chaulagain, C. Stehle, J. Larour, M. Kozlova, F. Suzuki-Vidal, P. Barroso, M. Cotelo, P. Velarde, R. Rodriguez, J.M. Gil, A. Ciardi, O. Acef, J. Nejdl, L. de Sa, R.L. Singh, L. Ibgui, N. Champion, Structure of a laser-driven radiative shock, High Energy Density Phys. 17 (2015) 106–113, https://doi.org/10.1016/j.hedp.2015.01.003.
[22] F. Suzuki-Vidal, T. Clayson, C. Stehle, G.F. Swadling, J.M. Foster, J. Skidmore, P. Graham, G.C. Burdiak, S.V. Lebedev, U. Chaulagain, R.L. Singh, E.T. Gumbrell, S. Patankar, C. Spindloe, J. Larour, M. Kozlova, R. Rodriguez, J. Gil, G. Espinosa, P. Velarde, C. Danson, Counter propagating radiative shock experiments on the Orion laser, Phys. Rev. Lett. 119 (2017), 055001, https://doi.org/10.1103/PhysRevLett.119.055001.
[23] F. Suzuki-Vidal, T. Clayson, C. Stehle, U. Chaulagain, J.W.D. Halliday, M.Y. Sun, L. Ren, N. Kang, H.Y. Liu, B.Q. Zhu, J.Q. Zhu, C.D. Rossi, T. Mihailescu, P. Velarde, M. Cotelo, J.M. Foster, C.N. Danson, C. Spindloe, J.P. Chittenden, C. Kuranz, First radiative shock experiments on the SG-II laser, High Power Laser Sci. Eng. 9 (2021) E27, https://doi.org/10.1017/hpl.2021.17.
[24] Y.T. Yuan, S.Y. Tu, C.A.S. Yin, J.W. Li, Z.S. Dai, Z.H. Yang, L.F. Hou, X.Y. Zhan, J. Yan, Y.S. Dong, Y. Pu, S. Zou, J.M. Yang, W.Y. Miao, Understanding effects of radiation from radiative shock on Richtmyer-Meshkov instability, Acta Phys. Sin. 70 (2021), 205203, https://doi.org/10.7498/aps.70.20210653.
[25] S. Colombo, L. Ibgui, S. Orlando, R. Rodriguez, G. Espinosa, M. Gonzalez, C. Stehle, G. Peres, Non-LTE radiation hydrodynamics in PLUTO, Astron. Astrophys. 631 (2019) A41, https://doi.org/10.1051/0004-6361/201935991.
[26] S. White, R. Irwin, J.R. Warwick, G.F. Gribakin, G. Sarri, F.P. Keenan, D. Riley, S. J. Rose, E.G. Hill, G.J. Ferland, B. Han, F. Wang, G. Zhao, Production of photoionized plasmas in the laboratory with X-ray radiation, Phys. Rev. E 97 (2018), 063203, https://doi.org/10.1103/PhysRevE.97.063203.
[27] F.W. Wang, G. Zhao, D. Salzmann, H. Nishimura, S. Fujioka, Y. Li, H. Takabe, J. Zhang, Comparison between simulated and experimental emission spectra of photoionizing nitrogen plasma, High Energy Density Phys. 5 (2009) 219–220, https://doi.org/10.1016/j.hedp.2009.05.007.
[28] I.M. Hall, T. Durmaz, R.C. Mancini, J.E. Bailey, G.A. Rochau, I.E. Golovkin, J. J. MacFarlane, Absorption spectroscopy of a laboratory photoionized plasmas at Z, Phys. Plasmas 21 (2014), 031203, https://doi.org/10.1063/1.4865226.

[29] J. Bauche, C. Bauche-Arnoult, O. Peyrusse, A. Bachelier, K.B. Fournier, C. Chenais-Popovics, J.C. Gauthier, Analysis of a non-LTE xenon spectrum by means of the model of superconfiguration temperatures, J. Quant. Spectrosc. Radiat. Transf. 81 (2003) 47–55, https://doi.org/10.1016/S0022-4073(03)00051-7.
[30] S. Bastiani-Ceccotti, N. Kontogiannopoulos, J.R. Marques, S. Tzortzakis, L. Lecherbourg, F. Thais, I. Matsushima, O. Peyrusse, Chenais-Popovics, Analysis of the x-ray and time-resolved XUV emission of laser produced Xe and Kr plasmas, High Energy Density Phys. 3 (2007) 20–27, https://doi.org/10.1016/j.hedp.2007.01.004.
[31] V.G. Novikov, V.V. Ivanov, K.N. Koshelev, V.M. Krivtsun, A.D. Solomyannaya, Calculation of tin emission spectra in discharge plasma: the influence of reabsorption in spectral lines, High Energy Density Phys. 3 (2007) 198–203, https://doi.org/10.1016/j.hedp.2007.02.014.
[32] M.J. May, M.B. Schneider, S.B. Hansen, H.K. Chung, D.E. Hinkel, H.A. Baldis, C. Constantin, X-ray spectral measurements and collisional-radiative modeling of hot, gold plasmas at the Omega laser, High Energy Density Phys. 4 (2008) 74–87, https://doi.org/10.1016/j.hedp.2008.07.001.
[33] J. Colgan, J.J. Abdallah, C.J. Fontes, D.P. Kilcrease, J. Dunn, M. Purvis, R.W. Lee, Non-LTE and gradient effects in K-shell oxygen emission laser-produced plasma, High Energy Density Phys. 6 (2010) 295–300, https://doi.org/10.1016/j.hedp.2010.01.015.
[34] E. Louzon, Z. Henis, I. Levy, G. Hurvitz, Y. Ehrlich, M. Frankel, S.M.E. Raicher, A. M.P. Mandelbaum, A. Zigler, Density diagnostic of highly ionized samarium laser produced plasma using Ni-like spatially resolved spectra, Laser Part. Beams 29 (2010) 61–67, https://doi.org/10.1017/S0263034610000765.
[35] E. Apaydin, M. Celik, Investigation of the plasma parameters of a laboratory argon plasma source using a collisional radiative model with the comparison of experimental and simulated spectra, Spectrochim. Acta B At. Spectrosc. 160 (2019), 105673, https://doi.org/10.1016/j.sab.2019.105673.
[36] K.B. Chai, D.H. Kwon, Optical emission spectroscopy and collisional-radiative modeling for non-equilibrium, low temperature helium plasma, Spectrochim. Acta B At. Spectrosc. 183 (2021), 106269, https://doi.org/10.1016/j.sab.2021.106269.
[37] L. Rachdi, V. Sushkov, M. Hofmann, Optical emission spectroscopy diagnostics for plasma parameters investigation in a duo-plasmaline surface-wave sustained discharge, Spectrochim. Acta B At. Spectrosc. 194 (2022), 106432, https://doi.org/10.1016/j.sab.2022.106432.
[38] X. Han, P. Wu, Z. Chen, J. Qi, Y. Wang, S. Lu, Y. Cui, H. Tang, J. Cao, Collisional radiative model for high-ionization-rate equilibrium argon plasma plume, Spectrochim. Acta B At. Spectrosc. 194 (2022), 106436, https://doi.org/10.1016/j.sab.2022.106436.
[39] R. Bates, A. Kingston, R. McWirther, Recombination between electrons and atomic ions, I. optically thin plasmas, Proc. R. Soc. London Ser. A 267 (1962) 297–312.
[40] J.P. Apruzese, J.L. Giuliani, Multi-dimensional radiation transport for modeling antisymmetric z pinches: ray tracing compared to Monte Carlo solutions for a two-level atom, J. Quant. Spectrosc. Radiat. Transf. 111 (2010) 134–143, https://doi.org/10.1016/j.jqsrt.2009.06.007.
[41] R. Rodriguez, G. Espinosa, G. J. M, MIXKIP/RAPCAL: a computational package for integrated simulations of large-scale atomic kinetics and radiation transport in non-local thermodynamic equilibrium plasmas, Comm. Comput. Phys. 30 (2021) 602–634, https://doi.org/10.4208/CICP.OA-2020-0264.
[42] G.C. Pomraning, The Equations of Radiation Hydrodynamics, Pergamon Press, New York, 1973.
[43] H.P. Jones, A. Skumanich, The formation of resonance lines in multidimensional media. II. Radiation operators and their numerical representation, Astrophys. J. 185 (1973) 167–182, https://doi.org/10.1086/152406.
[44] H.P. Jones, The formation of resonance lines in multidimensional media. III. Interpolation functions, accuracy, and stability, Astrophys. J. 185 (1973) 183–196, https://doi.org/10.1086/152407.
[45] R. Rodriguez, R. Florido, J.M. Gil, J.G. Rubiano, P. Martel, E. Minguez, RAPCAL code: a flexible package to compute radiative properties for optically thin and thick low and high-Z plasmas in a wide range of density and temperature, Laser Part. Beams 26 (2008) 433–448, https://doi.org/10.1017/S026303460800044X.
[46] R. Rodriguez, R. Florido, J.M. Gil, J.G. Rubiano, D. Suarez, P. Martel, E. Minguez, R.C. Mancini, Collisional-radiative calculations of optically thin and thick plasmas using the computational package ABAKO/RAPCAL, Commun. Comput. Phys. 8 (2010) 185–210, https://doi.org/10.4208/cicp.040809.231109a.
[47] E. Minguez, R. Florido, R. Rodriguez, J.M. Gil, J.G. Rubiano, M.A. Mendoza, D. Suarez, P. Martel, Opacity calculation for target physics using the ABAKO/RAPCAL code, High Energy Density Phys. 6 (2010) 57–65, https://doi.org/10.1016/j.hedp.2009.05.016.
[48] J.M. Gil, R. Rodriguez, P. Martel, R. Florido, J.G. Rubiano, M.A. Mendoza, E. Minguez, Analysis of the influence of the plasma thermodynamic regime in the spectrally resolved and mean radiative opacity calculations of carbon plasmas in a wide range of density and temperature, J. Quant. Spectrosc. Radiat. Transf. 114 (2013) 136–150, https://doi.org/10.1016/j.jqsrt.2012.05.016.
[49] J.M. Gil, R. Rodriguez, R. Florido, J.G. Rubiano, M.A. Mendoza, A. de la Nuez, G. Espinosa, P. Martel, E. Minguez, Parametrization of the average ionization and radiative cooling rates of carbon plasmas in a wide range of density and temperature, J. Quant. Spectrosc. Radiat. Transf. 125 (2013) 123–138, https://doi.org/10.1016/j.jqsrt.2013.02.015.
[50] R. Rodriguez, G. Espinosa, J. Gil, Radiative properties for astrophysical plasma mixtures in nonlocal thermodynamic equilibrium, Phys. Rev. E 98 (2018), 033213, https://doi.org/10.1103/PhysRevE.98.033213.
[51] R. Rodriguez, G. Espinosa, J.M. Gil, P.R. Beltran, Monochromatic and mean radiative properties of astrophysical plasma mixtures in nonlocal thermodynamic equilibrium regime, X Ray Spectr. 49 (2020) 6–10, https://doi.org/10.1002/xrs.2997.
[52] G. Espinosa, R. Rodriguez, J.M. Gil, Analysis of radiative opacities for optically thin and thick astrophysical plasmas, J. Quant. Spectrosc. Radiat. Transf. 237 (2019), 106633, https://doi.org/10.1016/j.jqsrt.2019.106633.
[53] R. Florido, T. Nagayama, R.C. Mancini, R. Tommasini, J.A. Delettrez, S.P. Regan, V.A. Smalyuk, R. Rodriguez, J.M. Gil, Analysis of time-resolved argon line spectra from omega direct-drive implosions, Rev. Sci. Instrum. 79 (2008) 10E310, https://doi.org/10.1063/1.2965779.
[54] R. Florido, R. Mancini, T. Nagayama, R. Tommasini, J.A. Delettrez, S.P. Regan, V. A. Smalyuk, R. Rodriguez, J.M. Gil, Argon k-shell and bound-free emission from Omega direct-drive implosion cores, High Energy Density Phys. 6 (2010) 70–75, https://doi.org/10.1016/j.hedp.2009.06.011.
[55] J.J. Abdallah, J. Colgan, N. Rohringer, Time-dependent calculations of electron energy distribution functions for neon gas in the presence of intense XFEL radiation, J. Phys. B 46 (2013), 235004, https://doi.org/10.1088/0953-4075/45/3/035701.
[56] R. Florido, R. Rodriguez, J.M. Gil, J.G. Rubiano, P. Martel, E. Minguez, R. C. Mancini, Modeling of population kinetics of plasmas that are not in local-thermodynamic equilibrium, using a versatile collisional-radiative model based on analytical rates, Phys. Rev. E 80 (2009), 056402, https://doi.org/10.1103/PhysRevE.80.056402.
[57] M.F. Gu, The flexible atomic code, Can. J. Phys. 86 (2008) 675–689, https://doi.org/10.1139/p07-197.
[58] D. Mihalas, B. Weible-Mihalas, Foundations of Radiation Hydrodynamics, Dover Publications Inc., New York, 1999.
[59] J. Bauche, C. Bauche-Arnoult, M. Klapisch, Transition arrays in the spectra of ionized atoms, Adv. At. Mol. Phys. 23 (1987) 131–195, https://doi.org/10.1016/S0065-2199(08)60107-4.
[60] M.S. Dimitrijevic, N. Konjevic, Simple estimates for stark-broadening of ion lines in stellar plasmas, Astron. Astrophys. 172 (1987) 345–349.
[61] J.C. Stewart, K.D. Pyatt, Lowering of ionization potentials in plasmas, Astrophys. J. 144 (1966) 1203–1211.
[62] M. Klapisch, M. Busquet, Models for the computation of opacity of mixtures, New J. Phys. 15 (2013), 015012, https://doi.org/10.1088/1367-2630/15/1/015012.
[63] S.B. Hansen, C.J. Fontes, J. Colgan, J.J. Abdallah, H.K. Chung, H.A. Scott, V. G. Novikov, O. Peyrusse, G.J. Ferland, R.J.R. Williams, Y. Ralchenko, Modern Methods in Collisional-Radiative Modeling of Plasmas, Springer, Berlin, 2016.
[64] R. Rodriguez, G. Espinosa, J.M. Gil, F. Suzuki-Vidal, C. Stehle, P. Graham, Analysis of microscopic properties of radiative shock experiments performed at the Orion laser facility, High Power Laser Sci. Eng. 6 (2018), e36, https://doi.org/10.1017/hpl.2018.28.
[65] F. Wang, S. Fujioka, H. Nishimura, D. Kato, Y. Li, G. Zhao, J. Zhang, H. Takabe, Experimental evidence and theoretical analysis of photoionized plasma under x-ray radiation produced by an intense laser, Phys. Plasmas 15 (2008), 073108, https://doi.org/10.1063/1.2946923.
[66] E.G. Hill, S.J. Rose, Modelling photoionised plasma experiments, High Energy Density Phys. 5 (2009) 302–306, https://doi.org/10.1016/j.hedp.2009.05.003.
[67] S.J. Rose, P.A.M. van Hoof, V. Jonauskas, F.P. Keenan, R. Kisielius, C. Ramsbottom, M.E. Foord, R.F. Heeter, P.T. Springer, Calculation of photoionized plasmas with an average-atom model, J. Phys. B Atom. Mol. Opt. Phys. 37 (2004) L337, https://doi.org/10.1088/0953-4075/37/17/L05.
[68] S.J. Rose, The effect of a radiation field on excitation and ionisation in non-LTE high energy density plasmas, High Energy Density Phys. 5 (2009) 23–26, https://doi.org/10.1016/j.hedp.2009.02.002.
[69] https://nlte.nist.gov/nlte8/.
[70] M.E. Foord, R.F. Heeter, P.A.M. van Hoof, R.S. Thoe, J.E. Bailey, M.E. Cuneo, H. K. Chung, D.A. Liedahl, K.B. Fournier, G.A. Chandler, V. Jonauskas, R. Kisielius, L. P. Mix, C. Ramsbotton, P.T. Springer, F.P. Keenan, S.J. Rose, W.H. Goldstein, Charge-state distributions and doppler effect in an expanding photoionized plasma, Phys. Rev. Lett. 93 (2004), 055002, https://doi.org/10.1103/PhysRevLett.93.055002.
[71] S.J. Rose, The non-LTE excitation/ionization code GALAXY, J. Phys. B Atom. Mol. Opt. Phys. 31 (1998) 2129–2144.
[72] D.R. Symes, H.W. Hohenberger, H. Doyle, R.A. Smith, A.S. Moore, E.T. Gumbrell, R. Rodriguez, J.M. Gil, Studying radiative shocks using laser driven blast waves in clustered gases, Nucl. Instrum. Methods Phys. Res. Sect. A 653 (2011) 186, https://doi.org/10.1016/j.nima.2010.12.050.
[73] J.J. MacFarlane, I.E. Golovkin, P.R. Woodruff, HELIOS-CR: a 1D radiation-magnetohydrodynamics code with inline atomic kinetics modelling, J. Quant. Spectrosc. Radiat. Transf. 99 (2013) 381–397, https://doi.org/10.1016/j.jqsrt.2005.05.031.
[74] R. Rodriguez, G. Espinosa, J.M. Gil, C. Stehle, F. Suzuki-Vidal, J.G. Rubiano, P. Martel, E. Minguez, Microscopic properties of xenon plasmas for density and temperature regimes of laboratory astrophysics experiments on radiative shocks, Phys. Rev. E 91 (2015), 053106, https://doi.org/10.1103/PhysRevE.91.053106.
[75] T. Ditmire, K. Shigemori, B.A. Remington, K. Estabrook, R.A. Smith, The production of strong blast waves through intense laser irradiation of atomic clusters, Astrophys. J. Suppl.Ser. 127 (2000) 299–304, https://doi.org/10.1086/313357.
[76] R. Rodriguez, G. Espinosa, J.M. Gil, R. Florido, J.G. Rubiano, M.A. Mendoza, P. Martel, E. Minguez, D.R. Symes, M. Hohenberger, R.A. Smith, Analysis of microscopic magnitudes of radiative blast waves launced in xenon clusters with collisional-radiative steady-state simulations, J. Quant. Spectrosc. Radiat. Transf. 125 (2013) 69–83, https://doi.org/10.1016/j.jqsrt.2013.03.019.